Effects of LGM sea surface temperature and sea ice extent on the isotope-temperature slope at polar ice core sites

Alexandre CAUQUOIN[1], Ayako ABE-OUCHI[2], Takashi OBASE[2], Wing-Le CHAN[3], André PAUL[4] and Martin WERNER[5]

[1]Institute of Industrial Science (IIS), The University of Tokyo, Kashiwa, Japan
[2]Atmosphere and Ocean Research Institute (AORI), The University of Tokyo, Kashiwa, Japan
[3]Research Center for Environmental Modeling and Application, Japan Agency for Marine-Earth Science and Technology (JAMSTEC), Yokohama, Japan
[4]MARUM – Center for Marine Environmental Sciences and Department of Geosciences, University of Bremen, Bremen, Germany
[5]Alfred Wegener Institute (AWI), Helmholtz Centre for Polar and Marine Sciences, Bremerhaven, Germany

Correspondence to: Alexandre Cauquoin (cauquoin@iis.u-tokyo.ac.jp)

Abstract. Stable water isotopes in polar ice cores are widely used to reconstruct past temperature variations over several orbital climatic cycles. One way to calibrate the isotope-temperature relationship is to apply the present-day spatial relationship as a surrogate for the temporal one. However, this method leads to large uncertainties because several factors like the sea surface conditions or the origin and the transport of water vapor influence the isotope-temperature temporal slope. In this study, we investigate how the sea surface temperature (SST), the sea ice extent and the strength of the Atlantic Meridional Overturning Circulation (AMOC) affect these temporal slopes in Greenland and Antarctica for Last Glacial Maximum (LGM, ~21 000 years ago) to preindustrial climate change. For that, we use the isotope-enabled atmosphere climate model ECHAM6-wiso, forced with a set of sea surface boundary condition datasets based on reconstructions (e.g., GLOMAP) or MIROC 4m simulation outputs. We found that the isotope-temperature temporal slopes in East Antarctic coastal areas are mainly controlled by the sea ice extent, while the sea surface temperature cooling affects more the temporal slope values inland. On the other hand, ECHAM6-wiso simulates the impact of sea ice extent on EDC and Vostok sites through the contribution of water vapor from lower latitudes. Effects of sea surface boundary condition changes on modeled isotope-temperature temporal slopes are various in West Antarctica. This is due partly to the transport of water vapor from the Southern Ocean to this area that can dampen the influence of local temperature on the changes in the isotopic composition of precipitation and snow. In the Greenland area, the isotope-temperature temporal slopes are influenced by the sea surface temperatures near the coasts of the continent. The greater the LGM cooling off the coast of southeast Greenland, the greater the transport of water vapor from the North Atlantic, and the larger the temporal slopes. The presence or absence of sea ice very near the coast has a large influence in Baffin Bay and the Greenland Sea and influences the slopes at some inland ice core stations. The extent of the sea ice far south slightly influences the temporal slopes in Greenland through the transport of more depleted water vapor from lower latitudes to this area. The seasonal variations of sea ice distribution, especially its retreat in summer, influence the isotopic composition of the water vapor in this region and the modeled isotope-temperature temporal slopes in the eastern part of

Greenland. A stronger LGM AMOC decreases LGM to preindustrial isotopic anomalies in precipitation in Greenland,
35   degrading the isotopic model-data agreement. The AMOC strength modifies the temporal slopes over inner Greenland slightly,
and by a little on the coasts along the Greenland Sea where the changes in surface temperature and sea ice distribution due to
the AMOC strength mainly occur.

1 Introduction

Stable isotopologues of water ($H_2^{16}O$, $H_2^{18}O$ and $HD^{16}O$, called hereafter stable water isotopes) are integrated tracers of climate
40   processes occurring in diverse parts of the hydrological cycle (Craig and Gordon, 1965; Dansgaard, 1964). Because of their
differences in mass and symmetries, an isotopic fractionation happens at each phase change of water. This process is reflected
by a change in the water isotope ratio values, expressed hereafter in the usual δ notation (as $\delta^{18}O$ and δ^2H with respect to the
Vienna Standard Mean Ocean Water V-SMOW if not stated otherwise). As a result, water isotopes have been widely used to
describe past variations of the Earth's climate. For example, their measurements in polar ice cores made it possible to
45   reconstruct the temperature variations over several glacial-interglacial cycles (Jouzel et al., 2007; Jouzel, 2013, and references
therein; NEEM Community Members, 2013).

For such a reconstruction, the present-day isotope-temperature spatial slope can be taken as a surrogate for the temporal
gradient at a given site. For example, a spatial slope of 0.80 ‰ °C^{-1} for $\delta^{18}O$ in Antarctica was calculated based on a compilation
of measured surface temperatures and $\delta^{18}O$ of snow at various locations in the continent (Masson-Delmotte et al., 2008).
50   However, this method often leads to a large error in the temperature reconstructions because the temporal isotope-temperature
slope depends on many factors like the sea surface temperature (SST) (Risi et al., 2010), the sea ice extent (Noone and
Simmonds, 2004), the ice sheet elevation (Werner et al., 2018), the origin and the transport of water vapor (Casado et al.,
2018). For example, it has been suggested that the relationship between temperature and the isotopic signature for warmer
interglacial periods in East Antarctica can vary among ice core sites, with an error in the temperature reconstruction that can
55   reach up to 100 % (Sime et al., 2009; Cauquoin et al., 2015). In Greenland, the use of the spatial relationship between the $\delta^{18}O$
in Greenland ice core records and surface temperature to evaluate the local temperature variations during the last deglaciation
leads to a large uncertainty of a factor of 2 (Jouzel, 1999; Buizert et al., 2014). Recently, Buizert et al. (2021) proposed a
reconstruction of surface cooling in Antarctica during the Last Glacial Maximum (LGM, ~21 000 years ago) using borehole
thermometry and firn properties of different ice cores. Based on these results, they proposed new estimates of temporal $\delta^{18}O$-
60   temperature slopes at these ice core stations, varying from 0.8 to 1.45 ‰ °C^{-1}.

The LGM is a period with full glacial conditions and represents the beginning of the last deglaciation. It is one of the key
climate periods chosen by the Paleoclimate Modeling Intercomparison Project (PMIP, Kageyama et al., 2018, 2021) because
it allows to evaluate how well state-of-the-art models are able to simulate climate changes as large as those expected in the
future. In addition to being very different from the preindustrial climate (PI), the LGM period also offers a wealth of isotope

65 proxy data, including stable water isotopes in polar ice cores for an in-depth comparison with outputs from isotope-enabled models (Lee et al., 2008; Risi et al., 2010; Werner et al., 2016, 2018).

One way to capture the physical processes influencing the temporal isotope-temperature slope in polar regions is the use of Atmospheric General Circulation Models (AGCMs) equipped with prognostic stable water isotopes. Such models can simulate different climate conditions, like LGM and PI periods. Moreover, the use of isotope-enabled AGCMs in combination with

70 isotopic observations allows us to investigate the physical processes controlling the variations of isotopic delta values at a given site. This method makes it possible to estimate the temporal isotope-temperature slope for LGM to preindustrial climate change (Lee et al., 2008; Risi et al., 2010; Werner et al., 2018). Even if such models simulate various temporal isotope-temperature slopes, implying that processes like water vapor transport, post-depositional effects, or polar atmospheric boundary layer are poorly or not represented (Krinner et al., 1997; Werner et al., 2000; Casado et al., 2018), these models are

75 very useful for evaluating the sensitivity of the temporal slopes to parameters like the change of elevation (Werner et al., 2018). Ocean surface conditions are one of the factors that influences LGM-PI isotope changes (Risi et al., 2010; Noone and Simmonds, 2004). Two reconstructions of SST and one of sea ice extent during the LGM period have been released recently. Paul et al. (2021) reconstructed both the SST and the sea ice extent fields, based on faunal and floral assemblage data of the Multiproxy Approach for the Reconstruction of the Glacial Ocean Surface (MARGO) project and several recent estimates of

80 the LGM sea ice extent. The Data-Interpolation Variational Analysis (DIVA) software was used to optimally interpolate sparse SST reconstruction data. The resulting reconstruction was called GLOMAP (Glacial Ocean Map). Tierney et al. (2020) reconstructed the LGM SST field with a different method, by combining a large collection of geochemical proxies for sea surface temperature with simulations outputs from the isotope-enabled model iCESM1.2 (Brady et al., 2019) using an offline data assimilation technique to produce a field reconstruction of LGM temperatures. Tierney et al. (2020) LGM cooling is

85 globally larger than in GLOMAP (3.6°C and 1.7°C, respectively), with possible impacts on LGM to PI isotope changes and their temporal relationship with near surface air temperature. In addition, other SST and sea ice fields, with different characteristics compared to the reconstructions of LGM sea surface conditions described above, can be extracted from atmosphere-ocean coupled model simulations like MIROC 4m (Obase and Abe-Ouchi, 2019).

Are air temperatures near the surface and the isotopic composition of precipitation in the polar regions influenced by LGM to

90 PI changes in SST and sea ice distribution in the same way? What are the underlying dynamics, for example, in terms of changes in concentrations and transport of water vapor? To answer to these questions, we performed multiple simulations with the isotope-enabled AGCM ECHAM6-wiso driven by different LGM SST and sea ice boundary conditions. We evaluate the modeled LGM-PI $\delta^{18}O$ anomalies with available observations and we investigate how the SST and the sea ice extent patterns influence the model-data agreement on a global scale and at polar ice core stations. The influence of ocean circulation,

95 particularly the strength of the Atlantic Meridional Overturning Circulation (AMOC), on sea surface conditions and by extension on our modeled $\delta^{18}O$ of meteoric water is also investigated. Finally, the impacts of the sea surface boundary conditions on the $\delta^{18}O$-temperature slopes for LGM-to-preindustrial climate change are evaluated and discussed for Greenland and Antarctic ice core stations.

2 Methodology

2.1 ECHAM6-wiso

ECHAM6 (Stevens et al., 2013) is the sixth generation of the atmospheric general circulation model ECHAM, developed at the Max Planck Institute for Meteorology. It consists of a dry spectral-transform dynamical core, a transport model for scalar quantities other than temperature and surface pressure, a suite of physical parameterizations for the representation of diabatic processes, and boundary datasets for externalized parameters (trace gas and aerosol distributions, land surface properties, etc.). ECHAM6 forms the atmospheric component of the fully coupled Earth system model MPI-ESM (Giorgetta et al., 2013; Mauritsen et al., 2019). The implementation of the water isotopes in ECHAM6 as part of MPI-ESM has been described and evaluated in detail by Cauquoin et al. (2019b), and this model version has been labeled ECHAM6-wiso. At a later stage, Cauquoin and Werner (2021) updated the water isotope module of ECHAM6-wiso in several aspects. The supersaturation has been slightly re-tuned, the kinetic fractionation factors for the evaporation over the ocean are now assumed as independent of wind speed, and the isotopic content of snow on sea ice is taken into account for sublimation processes in sea ice covered regions. The latter leads to a stronger depletion of surface water vapor over such sea ice covered areas (while the surface temperature remains the same). As a consequence, this change is expected to contribute to a steeper temporal isotope-temperature slope over sea ice covered areas.

2.2 Sea surface temperature and sea ice extent boundary conditions for LGM conditions

2.2.1 SST

Tierney et al. (2020) SST reconstruction has a larger and more homogeneous cooling than GLOMAP, except for the high southern latitudes at which the Pacific sector cools more than the Atlantic sector (Figure 1). On the other hand, the LGM cooling in the Northern North Atlantic Ocean is stronger in GLOMAP than in Tierney et al. reconstruction (-5.4°C and -4.8°C, respectively, see Table 4 in Paul et al., 2021). These differences between the two SST reconstructions are due to the use of different proxy datasets for the reconstructions (geochemical proxies only for Tierney et al., MARGO dataset for GLOMAP) and to the methods applied to produce SST gridded maps from scattered observations (see Section 1). For their offline data assimilation technique, Tierney et al. (2020) used results from the coupled climate model iCESM1.2, which shows one of the largest cooling among the PMIP4 models (Figure 1b of Kageyama et al., 2021). In addition to these two reconstructions, we used SST and sea ice extent outputs from a MIROC 4m LGM simulation (Obase and Abe-Ouchi, 2019) with oscillating AMOC strength. The global LGM cooling is between -2.3 and -2.7°C according to the considered simulations (Figure 1) i.e., higher than GLOMAP and lower than the Tierney et al. reconstruction. The main specificity of MIROC 4m LGM SST is a very strong cooling in the North Atlantic (more than 10°C, Figure 1) and more uniform temperature anomalies between -2 and -4°C in the other areas, including off the coast of Greenland. We extracted the MIROC 4m SST outputs, averaged over a 100-year period, at two different times of the LGM simulation depending on the AMOC strength: during a weak AMOC phase (average AMOC index was equal to 8.44 Sv) and a strong AMOC phase (19.95 Sv). A weaker AMOC during LGM implies larger cooling in

the North Atlantic (Figure 1) and more extended sea ice (Figure 2), while it does less cooling in the Southern Ocean. The strong AMOC phase period in MIROC 4m simulation was selected in the middle of the AMOC peak (Figure S1). Therefore, the values of MIROC 4m average near surface air temperature in Antarctica are very similar regardless the selected AMOC phase. For example, MIROC 4m simulates LGM temperature of -41.87 and -41.75°C in WDC station for strong and weak AMOC phase, respectively. A similar pattern is found for the eastern part of the continent (-56.80 and -56.50°C in Dome Fuji for strong and weak AMOC phase, respectively).
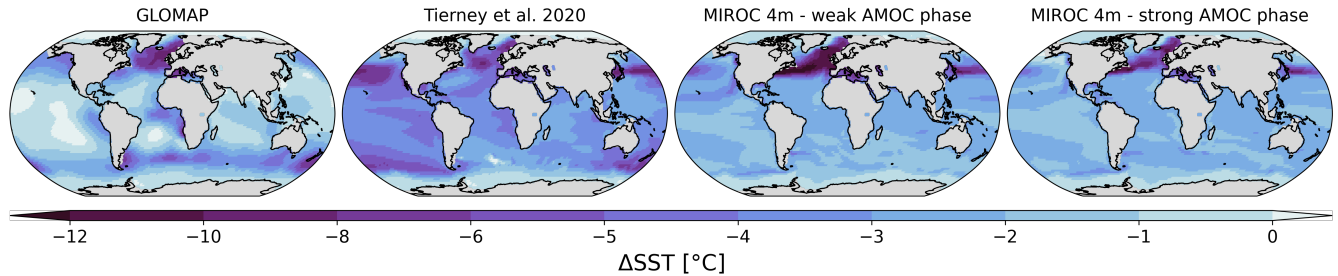
Figure 1: LGM-PI sea surface temperature changes used as boundary conditions for ECHAM6-wiso simulations. From left to right: GLOMAP (Paul et al., 2021), Tierney et al. (2020), MIROC 4m with weak LGM AMOC phase and MIROC 4m with strong LGM AMOC phase. Anomalies are expressed relative to Atmospheric Model Intercomparison Project mean SST over the period 1870 to 1899.

2.2.2 Sea ice extent

Maps of the averaged sea ice area fraction used as boundary forcings for ECHAM6-wiso are shown in Figure 2. The PI AMIP and LGM GLOMAP sea ice cover is higher around Antarctica compared to MIROC 4m ones, with a further extent in the Southern Ocean especially in the Atlantic sector. On the other hand, sea ice is more extensive in the Northern Hemisphere for MIROC 4m in the weak AMOC phase. For the stronger AMOC case, a decline of the sea ice in the Northern Hemisphere is seen, accompanied by weaker cooling (see section 2.2.1). In its parameterization, MIROC 4m uses a threshold of 95% for the sea ice fraction to allow sub-grid "sea-ice leads". This threshold is not rigid, but it is difficult to exceed sea ice concentrations of 95% unless there is significant convergence of sea-ice. Consequently, while the sea ice is, on average, more extensive in the north in MIROC 4m for the weak AMOC phase compared to GLOMAP reconstruction, the sea ice area fraction in grid cells near coastal areas like Greenland is lower in MIROC 4m than in GLOMAP (95-98% against 100%, respectively).
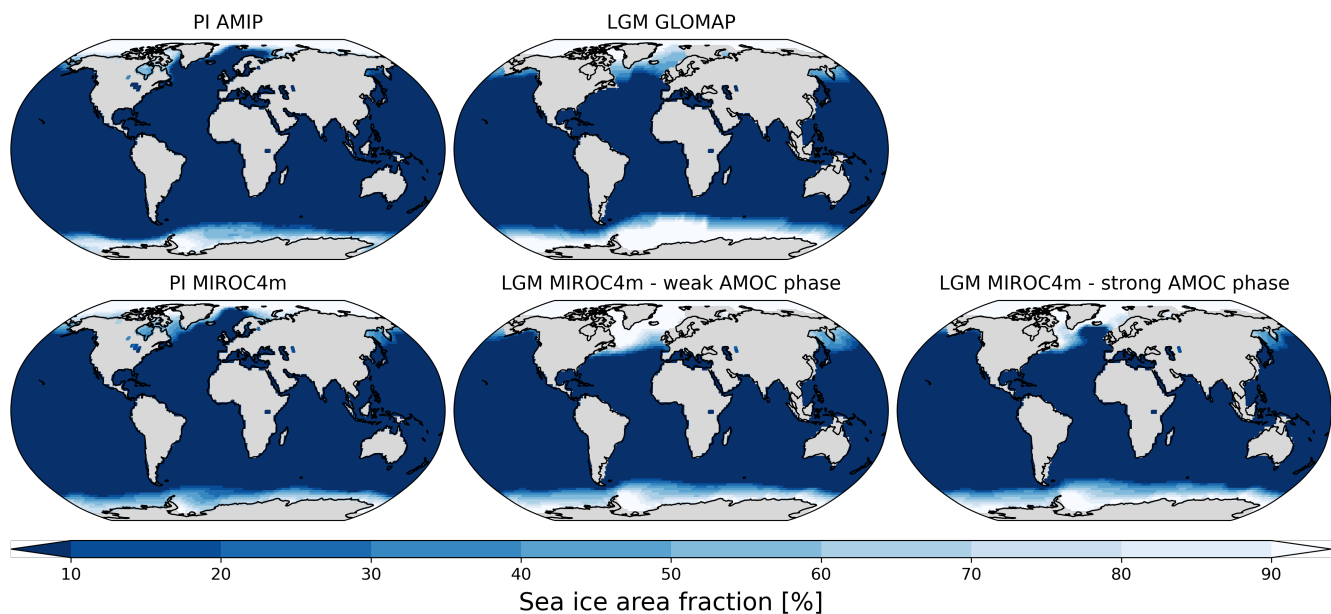
Figure 2: LGM and PI sea ice area fractions used as boundary conditions for ECHAM6-wiso simulations.

2.3 Model setup and experiments

155 We performed an ensemble of LGM simulations with ECHAM6-wiso, forced with different combinations of SST and sea ice boundary forcings presented in section 2.2. All our PI and LGM simulations are designed with respect to the PMIP4 protocol (e.g., greenhouse gas and orbital conditions). The LGM SST boundary fields are expressed relative to the Atmospheric Model Intercomparison Project (AMIP, Eyring et al., 2016) mean SST (averaged over the period 1870 to 1899) used for the preindustrial simulations (Table 1). The GLOMAP reconstruction has the advantage of providing a monthly climatology of

160 LGM SST and sea ice extent, while only annual mean SST is available from the reconstruction by Tierney et al. (2020), without sea ice map distribution. So, Tierney et al. LGM SST for ECHAM6-wiso was produced by taking the annual mean SST anomaly from Tierney et al. (2020) and adopting the monthly climatology temperature variability from GLOMAP. Since we also used GLOMAP sea ice extent data in this case, the SST was adjusted slightly to maintain consistency (e.g., SST set to freezing temperature where there is sea ice). In order to investigate the impact of sea ice extent on our isotope results and the

165 related isotope-temperature slopes for LGM-to-PI climate change, we used LGM SST outputs from MIROC 4m simulations combined with sea ice extent data from the same MIROC 4m simulations or from GLOMAP dataset. To evaluate the LGM-PI anomalies, we performed several PI simulations with different sea ice boundary conditions depending on the setup of LGM experiments, using climatological monthly mean sea ice area fractions from AMIP or MIROC 4m coupled simulations (Table 1). The prescribed LGM ice sheet is GLAC-1D (Tarasov and Peltier, 2002; Tarasov et al., 2012, 2014; Abe-Ouchi et al., 2013;

170 Briggs et al., 2014) for all LGM simulations. As with SST and sea ice distribution, mean $\delta^{18}O$ of surface seawater needs to be prescribed. For the PI simulations, we used the $\delta^{18}O$ reconstruction from the global gridded data set of LeGrande and Schmidt

(2006). As no equivalent data set of the δ^2H composition of seawater exists, the deuterium isotopic composition of the seawater in any grid cell has been set equal to the related $\delta^{18}O$ composition, multiplied by a factor of 8, in accordance with the observed relation for meteoric water on a global scale (Craig, 1961). As in Werner et al. (2018), a prescribed glacial seawater enrichment of +1 ‰ and +8‰ is assumed for $\delta^{18}O$ and δ^2H in the LGM simulations, respectively. The PI and LGM simulations were run for 60 and 120 model years, respectively, and we used the last 30 model years for our analyses. The simulations' characteristics are summarized in Table 1. Two additional sensitivity simulations have been performed to evaluate the impacts of lower MIROC 4m sea ice area fraction in coastal grid cells (section 2.2.2) and the consideration of the isotopic composition of snow on sea ice in ECHAM6-wiso (section 2.1) on the modeled $\delta^{18}O_p$-temperature temporal slopes between LGM and PI (see Supplementary Text S1). Also, a LGM simulation using the PMIP3 ice sheet reconstruction instead of GLAC-1D (see Figures 3b and 3d of Werner et al. (2018), respectively) has been performed to evaluate the impact of ice sheet topography on the isotopically enriched bias in Antarctica (Supplementary Text S1).

Table 1: Characteristics of the ECHAM6-wiso simulations in the present study.

LGM simulation name	SST	Sea ice	PI control simulation characteristics	Comments
LGM_GLOMAP	GLOMAP	GLOMAP	Mean PI SST and sea ice from AMIP	Less global SST cooling
LGM_tierney2020	Tierney et al., 2020	GLOMAP	Mean PI SST and sea ice from AMIP	More global SST cooling
LGM_miroc4m_sst_glomap_sic	MIROC 4m	GLOMAP	Mean PI SST and sea ice from AMIP	AMOC oscillation: weak phase
LGM_miroc4m_sst_and_sic	MIROC 4m	MIROC 4m	Mean PI SST from AMIP and PI sea ice from MIROC 4m	AMOC oscillation: weak phase
LGM_miroc4m_strong_AMOC_sst_glomap_sic	MIROC 4m	GLOMAP	Mean PI SST and sea ice from AMIP	AMOC oscillation: strong phase
LGM_miroc4m_strong_AMOC_sst_and_sic	MIROC 4m	MIROC 4m	Mean PI SST from AMIP and PI sea ice from MIROC 4m	AMOC oscillation: strong phase

2.4 Observational data

To evaluate the modeled $\delta^{18}O$ of precipitation and snow values at ice core stations, we use here a selection of 6 Greenland and 11 Antarctic ice cores for the preindustrial and LGM climates (Figure 3). The observed $\delta^{18}O$ values were defined as averages over the last 200 years for the preindustrial period, and in the 21 ± 1 ka period for the LGM. We also use LGM-PI $\delta^{18}O$ anomalies from 5 (sub-)tropical ice cores that are reported in Table 2 of Risi et al. (2010). The ice core data used in this study are summarized in Table 2. Similarly, we use temperature reconstructions based on borehole reconstructions or $\delta^{15}N$ at 7 Antarctic and one Greenland ice cores (Buizert et al., 2021; Dahl-Jensen et al., 1998) to evaluate the air surface temperatures near the surface, as modeled by ECHAM6-wiso. In order to mitigate the seasonal bias when comparing observed $\delta^{18}O$ from snow in ice cores with modeled $\delta^{18}O$ of precipitation or deposited snow, the modeled δ values are calculated as a precipitation (or snow)-weighted mean with respect to the V-SMOW scale. For the evaluation of modeled $\delta^{18}O$ of precipitation at a global

spatial scale, we extracted 14 entities from the SISALv2 speleothem dataset (Comas-Bru et al., 2020) where both PI and LGM
δ¹⁸O values of calcite or aragonite are available (see Supplementary Text S2 for the details).
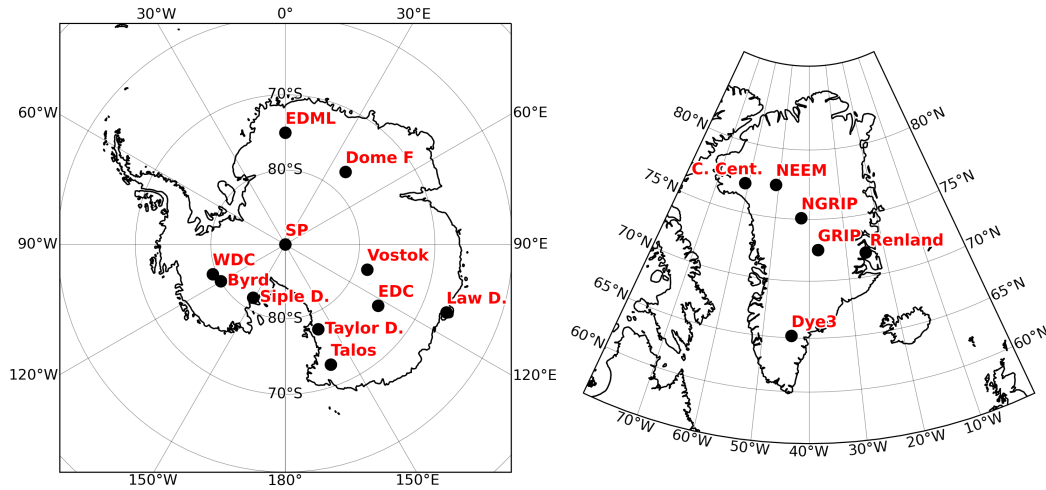
Figure 3: Location of polar ice core sites in Antarctica (left) and Greenland (right).

Table 2: Selected ice cores records and their geographical coordinates, reported PI values of δ¹⁸O, changes in δ¹⁸O between LGM and PI and modeled range of Δδ¹⁸O among our simulations reported in Table 1.

Site	Longitude	Latitude	δ¹⁸O$_{PI}$ (‰)	Δδ¹⁸O (‰)	Modeled Δδ¹⁸O range (‰)
South Pole[a]	0	-90	-51.0	-6.4	-3.33 ; -0.65
Vostok[b,c]	106.87	-78.47	-56.8	-4.8	-2.45 ; -0.08
Dome F[d]	39.70	-77.32	-54.6	-4.9	-2.75 ; -0.37
EDC[e,f]	123.35	-75.10	-50.4	-5.6	-2.30 ; 0.48
EDML[c,e]	0.07	-75.00	-44.8	-6.3	-3.95 ; -0.91
Law Dome[c]	112.83	-66.73	-22.4	-5.5	-5.13 ; -0.27
Taylor Dome[g]	158.72	-77.8	-40.5	-3.5	-5.73 ; -2.87
Talos[h]	159.18	-72.82	-36.1	-5.4	-2.28 ; -0.37
Byrd[i]	-119.52	-80.02	-32.9	-7.3	-4.55 ; -1.40
Siple Dome[c]	-148.82	-81.67	-25.6	-7.8	-6.23 ; -3.23
WDC[c]	-112.14	-79.46	-34	-7.3	-5.03 ; -1.66
GRIP[b,k]	-37.63	72.58	-35.3	-5.4	-3.23 ; -0.43
NGRIP[b,l]	-42.32	75.10	-35.2	-7.4	-6.37 ; -3.71
NEEM[m,n]	-51.06	77.45	-33	-10	-6.48 ; -5.17
Camp Century[j]	-61.13	77.17	-29.3	-12.9	-9.40 ; -6.73
Dye3[k]	-43.81	65.18	-27.7	-7.3	-5.58 ; -3.79
Renland[j]	-25.00	72.00	-27.4	-3.8	-9.14 ; -5.72
Huascaran[b]	-77.61	-9.11	-	-6.3	-3.33 ; -0.65

Sajama[b]	-68.97	-18.1	-	-5.4	-2.45 ; -0.08
Illimani[b]	-67.77	-16.62	-	-6	-2.75 ; -0.37
Guliya[b]	81.48	35.28	-	-5.4	-2.30 ; 0.48
Dunde[b]	96	38	-	-2	-3.95 ; -0.91

References: reported in [a] Steig et al. (2021), [b] Risi et al. (2010), [c] WAIS Divide project members (2013), [d] Kawamura et al. (2007), [e] Stenni et al. (2010), [f] Landais et al. (2015), [g] Steig et al. (2000), [h] Stenni et al. (2011), [i] Blunier and Brook (2001), [j] Vinther et al. (2009), [k] Vinther et al. (2006), [l] North Greenland Ice Core project members (2004), [m] Guillevic et al. (2013), [n] Schüpbach et al. (2018).

3 Results of the LGM-PI ECHAM6-wiso simulations

3.1 Evaluation of ECHAM6-wiso under LGM conditions

We evaluate here the global distribution of $\delta^{18}O$ of precipitation ($\delta^{18}O_p$) changes between LGM and PI ($\Delta\delta^{18}O_p$) from our different ECHAM6-wiso simulations. Figure 4 shows the comparison of modeled $\delta^{18}O_p$ anomalies with isotope measurements from ice cores and speleothems for the simulation LGM_miroc4m_sst_and_sic (i.e., SST and sea ice boundary conditions from MIROC 4m simulation at weak AMOC phase). Well-known patterns of global $\Delta\delta^{18}O_p$ distribution are found in ECHAM6-wiso, like the negative anomalies across Canada, Greenland and Northern Europe due to the presence of glaciers in these areas during LGM period (Figure 4c). Generally, negative $\delta^{18}O_p$ anomalies are also simulated over Antarctica and the Southern Ocean, where the LGM cooling is stronger compared to lower southern latitudes (Figure 4a). In the mid-to-low latitudes, $\Delta\delta^{18}O_p$ is mainly controlled by precipitation anomalies (Figure 4b). For example, lower modeled precipitation in the Amazonian area, over parts of South East Asia and in the western Pacific Ocean during the LGM leads to positive modeled $\delta^{18}O_p$ anomalies. Despite some biases in modeled $\Delta\delta^{18}O_p$, like in Southern Amazonia (Figures 4c and d) where negative anomalies are measured in ice cores (between -2 and -6‰, see green dots in Figure 4d) while positive anomalies are simulated (between 0 and 4‰), modeled $\delta^{18}O_p$ anomalies are in rather good agreement with observations from ice cores and speleothems (Figure 4d).
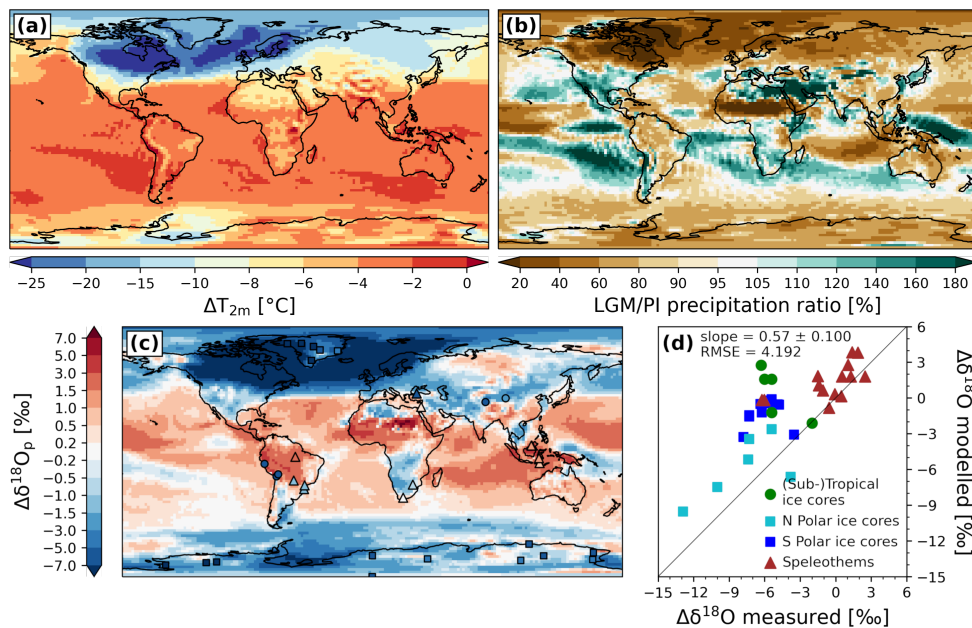
Figure 4: (a) LGM-PI 2m air temperature changes, (b) LGM/PI precipitation ratio and (c) LGM-PI $\delta^{18}O_p$ anomalies from the LGM_miroc4m_sst_and_sic simulation (background colors). In (c), the squares, dots and triangles represent $\delta^{18}O$ changes measured in polar ice cores, (sub-)tropical ice cores and speleothems, respectively. Measured $\delta^{18}O$ in calcite or aragonite from speleothems have been converted into $\delta^{18}O$ of drip-water before comparison with modeled $\delta^{18}O_p$ (see Section 2.4). (d) Scatter plot showing a comparison of observed $\delta^{18}O$ changes with modeled $\delta^{18}O_p$ anomalies at the nearest grid cell of the archives' locations. Northern and southern polar ice core locations are distinguished by cyan and blue colors, respectively.

The isotope fractionation is mainly controlled by changes in temperature and in the water cycle. Even though all the ECHAM6-wiso simulations show similar global distribution of 2m air temperature (T_{2m}) and precipitation responses to the various SST and sea ice boundary fields, we find some differences too (Figures S2 and S3 in Supplementary Material). As expected, the modeled global cooling using SST from GLOMAP is lower while it is stronger when using SST from Tierney et al. (2020) (cooling of -4 and -6.3°C, respectively). Average T_{2m} anomalies in the middle range are obtained when using the MIROC 4m SST fields (between -4.4 and -5.3°C depending on the MIROC 4m data used). The temperature over sea ice covered areas are largely impacted by the sea ice forcings used (i.e., GLOMAP or MIROC 4m). The modeled T_{2m} anomalies over the Southern Ocean vary between -10 and -15°C with an extensive LGM sea ice (GLOMAP) while the cooling is only between -4 and -10°C when ECHAM6-wiso is forced by a less extensive one (MIROC 4m sea ice). For the Arctic region, a strong cooling is simulated with the very extensive sea ice from MIROC 4m with a weak AMOC phase (a cooling of more than 20°C), more than with the sea ice from GLOMAP (between -20 and -10°C). The different SST boundary conditions have a strong influence on the precipitation anomalies, especially at mid-to-low latitudes including the western Pacific area and the East Asian monsoon region (Figure S3). All these differences in T_{2m} and precipitation responses have profound impacts on modeled $\delta^{18}O_p$ anomalies (Figure S4) and their agreements with observations (Figures 4c and d).

Table 3: Values of Δδ¹⁸O model-data slope (1 is better), coefficient of determination r^2 and root mean square error (RMSE) for our ECHAM6-wiso simulations using different SST and sea ice boundary fields. For each column, worst to best model-data agreements are shown with a yellow-to-green colormap.

LGM simulation name	Slope	r^2	RMSE (‰)
LGM_GLOMAP	0.699	0.543	3.938
LGM_tierney2020	0.646	0.588	3.500
LGM_miroc4m_sst_glomap_sic	0.589	0.561	3.930
LGM_miroc4m_sst_and_sic	0.574	0.490	4.192
LGM_miroc4m_strong_AMOC_sst_glomap_sic	0.656	0.579	3.931
LGM_miroc4m_strong_AMOC_sst_and_sic	0.551	0.527	4.348

The statistics of Δδ¹⁸O$_p$ model-data agreements are shown for our different ECHAM6-wiso simulations in Table 3. The best model-data agreement in terms of model-data slope (1 is perfect match) is found when using SST and sea ice from GLOMAP (slope = 0.70) as boundary conditions for ECHAM6-wiso, but better coefficient of determination (r^2) and root mean square error (RMSE) are obtained with LGM SST from Tierney et al. (2020) (r^2 = 0.58 and RMSE = 3.5 ‰). We notice a worse model-data agreements in δ¹⁸O$_p$ changes when both SST and sea ice changes from MIROC 4m simulations are provided as sea surface boundary conditions (slopes lower than 0.582 and RMSE higher than 4.1 ‰). This is in agreement with Werner et al. (2018) who showed a worse model-data agreement when using SST and sea ice boundary conditions from a coupled model instead of reconstructed ones. The substitution of MIROC 4m sea ice changes by GLOMAP ones, which are more extensive in the south and less extensive in the north, improves the Δδ¹⁸O$_p$ model-data agreement for all cases (i.e., weak or strong AMOC phase). For example, the model-data slope when using SST changes from MIROC 4m simulation during strong AMOC phase is similar to the one for the simulation with the Tierney et al. SST reconstruction (0.66 and 0.65, respectively).

3.2 Impacts of SST boundary conditions on the Δδ¹⁸O model-data agreement at polar ice core stations

The modeled values of Δδ¹⁸O of snow (δ¹⁸O$_{sn}$) and ΔT$_{2m}$ at polar ice cores stations for different boundary conditions in LGM-PI SST changes are compared to isotopic observations and temperature reconstructions in Figure 5a. Only simulations using sea ice from GLOMAP are selected here. Except for Renland station in the North and Taylor Dome in the South (that are both coastal sites), ECHAM6-wiso generally under-estimates δ¹⁸O$_{sn}$ changes. We find a generally good agreement with the reconstructed temperature data, except for GRIP station where the cooling is 6-10°C too weak (dots and crosses in Figure 5a). The substitution of GLAC-1D reconstruction by the PMIP3 one strongly improves the model-data agreement of δ¹⁸O in Antarctica (Figure S5), leading to a better model-data agreement at global scale (slope = 0.87, r^2 = 0.62 and RMSE = 3.2 ‰) compared to the LGM_GLOMAP experiment. This agrees with the findings of Werner et al. (2018) who showed that the isotopic model-data correlation for Antarctic ice core stations is weaker when using GLAC-1D instead of PMIP3 ice sheet reconstruction (RMSE = 2.1 and 1.1 ‰ for 11 Antarctic stations, respectively). However, this better Δδ¹⁸O model-data

265 agreement is more likely due to a bias compensation than a more realistic ice sheet because the simulation of Antarctic temperatures by ECHAM6-wiso is degraded at the same time (markers in Figure S5). Except for the Taylor Dome station, all modeled $\Delta\delta^{18}O_{sn}$ at polar ice core stations are in better agreement with measurements (blue bars in Figure 5a) when reconstructed SST fields (i.e., GLOMAP or Tierney et al.) are used (orange and green bars in Figure 5a, respectively), confirming the results of Werner et al. (2018) about the worse model-data agreement when using sea surface boundary

270 conditions from a coupled model instead of reconstructed ones. The change from one MIROC 4m SST field to another one (i.e., weak or strong AMOC phase) as input for ECHAM6-wiso does not modify the modeled $\Delta\delta^{18}O_{sn}$ values much (red and purple bars in Figure 5a).

For a stronger SST cooling in the Southern Ocean (GLOMAP and Tierney et al.), ECHAM6-wiso simulates higher $\delta^{18}O_p$ changes (right maps of Figure 5) that are in better agreement with the observations. A stronger cooling in the Atlantic sector

275 of the Southern Ocean (GLOMAP SST compared to the Tierney et al. one) has the consequence of enhancing the $\delta^{18}O_p$ depletion in the Atlantic-Indian Ocean sector of Antarctica (right map of Figure 5c) despite similar temperatures (left map of Figure 5c). This area includes the ice core stations Dome Fuji and EDML, where better $\delta^{18}O$ and similar temperature model-data agreements are found (orange markers and bars in Figure 5a). This is also true for other stations further to the east and west, like WDC and EDC (green bars and markers in Figure 5a). When using a SST field with stronger cooling in the Northern

280 North Atlantic Ocean (i.e., GLOMAP), a stronger cooling is simulated there to the south of Greenland. A stronger cooling is simulated in the southern and central parts of inner Greenland too (left maps of Figure 5) with consequently higher $\delta^{18}O$ changes between LGM and PI in Greenland (right maps of Figure 5) except in Northern part like at Camp Century station (Figure 5a). A better agreement is obtained with the Greenland $\delta^{18}O$ observations under this configuration (orange bars in Figure 5a), without improving the overly too weak cooling in the model (colored markers for GRIP station in Figure 5a).
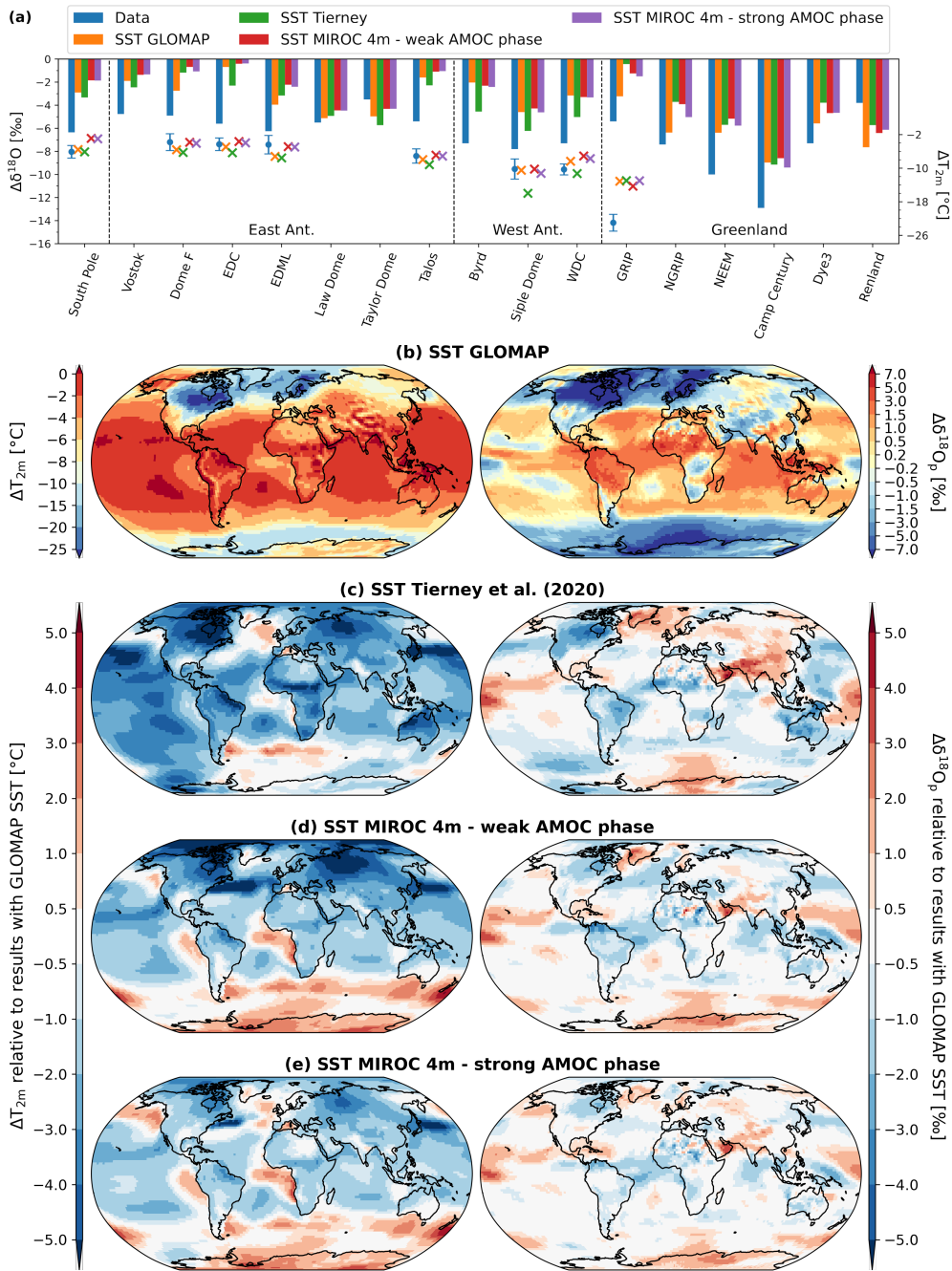
Figure 5: (a) Comparison of modeled anomalies in T_{2m} (crosses, right vertical axis) and $\delta^{18}O_{sn}$ (bars, left vertical axis) between LGM and PI with temperature and $\delta^{18}O$ anomalies from polar ice cores (blue dots and bars, respectively). All modeled results are from simulations with the same sea ice boundary conditions from GLOMAP but with different SST forcings: GLOMAP (orange), Tierney et al. (2020) (green), MIROC 4m with weak LGM AMOC phase (red) and MIROC 4m with strong LGM AMOC phase (purple). **(b)** Modeled T_{2m} and $\delta^{18}O_p$ changes between LGM and PI using GLOMAP SST (left and right maps, respectively). Maps in plots **(c)** to **(e)** show the impacts on T_{2m} and $\delta^{18}O_p$ anomalies using the other SST boundary conditions. The values are expressed relative to the modeled results from **(b)**.

285

290

3.3 Impacts of sea ice changes boundary conditions on the $\Delta\delta^{18}O$ model-data agreement at polar ice core stations

To analyze the effects of sea ice boundary conditions on the modeled $\delta^{18}O$ changes in polar regions between LGM and PI, we compare the results from the simulations using the same SST (here from the MIROC 4m simulation with the weak AMOC phase) but different sea ice area fraction fields: GLOMAP and MIROC 4m (i.e., LGM_miroc4m_sst_glomap_sic and LGM_miroc4m_sst_and_sic simulations, respectively). For all Antarctic ice core stations, a stronger depletion in $\delta^{18}O_{sn}$ between LGM and PI is simulated when the LGM sea ice in the Southern Ocean is more extensive (GLOMAP, orange bars in Figure 6a). Except for Taylor Dome, a better agreement with isotopic observations is then found as well as a better agreement with temperature reconstructions in West Antarctica. It has a huge impact on modeled T_{2m} anomalies over the Southern Ocean (between 2 and 10°C), and the simulated cooling is higher by 1 to 4°C in Western Antarctica and in coastal regions of the continent (left map of Figure 6c). As a consequence, higher LGM-PI anomalies in $\delta^{18}O$ of precipitation and of snow are simulated: more than 5 ‰ over the Southern Ocean and around 1-2 ‰ on the continent, especially in the western part (right map of Figure 6c). A more extensive northern sea ice (i.e., MIROC 4m) increases the cooling by 5 to 10°C in the Arctic Ocean and from 0.5 to 5 °C in Greenland (left map of Figure 6c), giving higher $\delta^{18}O_p$ anomalies of up to 2 ‰ (right map of Figure 6c) generally in better agreement with the temperature and $\delta^{18}O$ observations (green bars and markers in Figure 6a). The opposite is true with the less extensive sea ice distribution from MIROC 4m under a strong AMOC phase, weakening the model-data agreement for Greenland (Figure S6). Smaller sea ice area fraction in grid cells near coastal areas in MIROC 4m compared to GLOMAP (95-98% against 100%, respectively. See section 2.2.2), resulting in less important LGM-PI sea ice change, makes the cooling near the Greenland coast slightly lower. This lower sea ice change in MIROC 4m combined with the isotopic content of snow on sea ice taken into account for sublimation processes in sea ice covered regions leads to a reduction of the LGM-PI $\delta^{18}O_p$ changes in Baffin Bay (right map of Figure 6c). This aspect is investigated in detail in section 4.2.
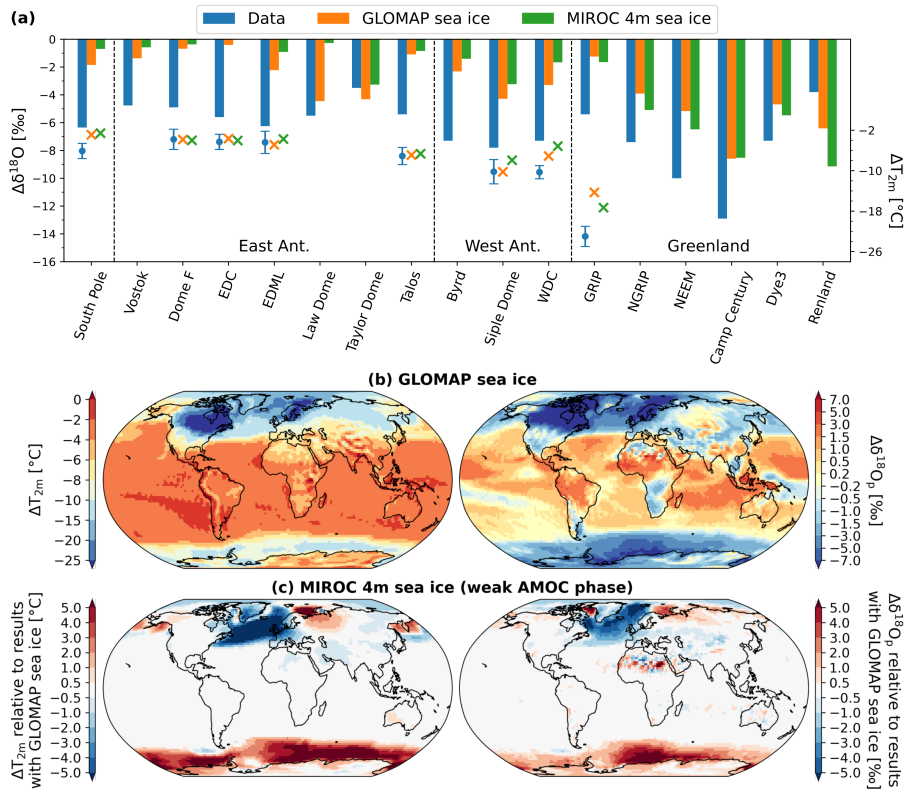
Figure 6: (a) Comparison of modeled anomalies in T_{2m} (crosses, right vertical axis) and $\delta^{18}O_{sn}$ (bars, left vertical axis) between LGM and PI with temperature and $\delta^{18}O$ anomalies from polar ice cores (blue dots and bars, respectively). Modeled results are from the simulations using the SST changes of MIROC 4m with weak LGM AMOC but different sea ice boundary conditions (GLOMAP and MIROC 4m with weak LGM AMOC phase in orange and green, respectively). **(b)** Modeled T_{2m} and $\delta^{18}O_p$ changes between LGM and PI using GLOMAP sea ice (left and right maps, respectively). Maps in **(c)** show the impacts on T_{2m} and $\delta^{18}O_p$ anomalies using sea ice from MIROC 4m instead. Values are expressed relative to the modeled results from (b).

3.4 Impacts of LGM AMOC strength on the $\Delta\delta^{18}O$ model-data agreement at polar ice core stations

Here, we investigate the impacts of AMOC strength on the modeled $\Delta\delta^{18}O$ in polar regions. For that, sea surface outputs (i.e., both SST and sea ice spatial distribution) from the MIROC 4m simulation with different LGM AMOC strengths are used as boundary conditions for ECHAM6-wiso. We focus first on the North Pole region because the AMOC strength mainly influences the climate of the Northern Hemisphere, as shown in SST and sea ice distributions used in this study (Figures 1 and 2). A weaker AMOC during LGM involves less heat transported in the north and thus lower LGM temperatures (i.e., larger cooling relative to PI), as shown in the left map of Figure 7c. A difference in T_{2m} of up to 10°C in the North Atlantic and Arctic Oceans is seen in the LGM_miroc4m_strong_AMOC_sst_glomap_sic and LGM_miroc4m_strong_AMOC_sst_and_sic simulations. Cooling in Greenland is reduced by 2 to 6 °C when the AMOC is increased, increasing the warm bias in GRIP (markers in Figure 7a). LGM to PI changes in $\delta^{18}O$ in Greenland is mainly controlled by this change in mean temperature with an increase in LGM $\delta^{18}O_{sn}$ of between 1.2 and 2.5 ‰ at Greenland ice core stations for a stronger LGM AMOC (orange and

green bar in Figure 7a). As ECHAM6-wiso generally underestimates the LGM-PI δ^{18}O changes at the poles, a weaker AMOC generally improves the model-data agreement (blue and orange bars in Figure 7a). In the Southern Ocean and Antarctic regions, only small T_{2m} changes are simulated by ECHAM6-wiso due to a change in AMOC strength during LGM (left map of Figure

335 7c), as shown by the absence of any effect on model-data temperature agreement (markers in Figure 7a). As a consequence, modeled $\Delta\delta^{18}O_{sn}$ values are very similar between the 2 simulations (orange and green bars in Figure 7a). These small differences are due to the selection of the strong AMOC phase period in the middle of the peak in MIROC 4m simulation (see section 2.2.1). The impact of the period selection for the strong AMOC phase (e.g., the start or the end of the interstadial) on surface temperature and δ^{18}O in Antarctica will be investigated more in detail in a future study. Finally, the changes of SST

340 values alone due to AMOC strength variations change by only less than 1 ‰ of the modeled $\Delta\delta^{18}O_{sn}$ (red and purple bars in Figure 5a). This shows that the LGM to PI changes in sea ice distribution, related to the AMOC strength variations, have a large impact on modeled T_{2m} anomalies and consequently on the isotopic signals in the North Pole region.
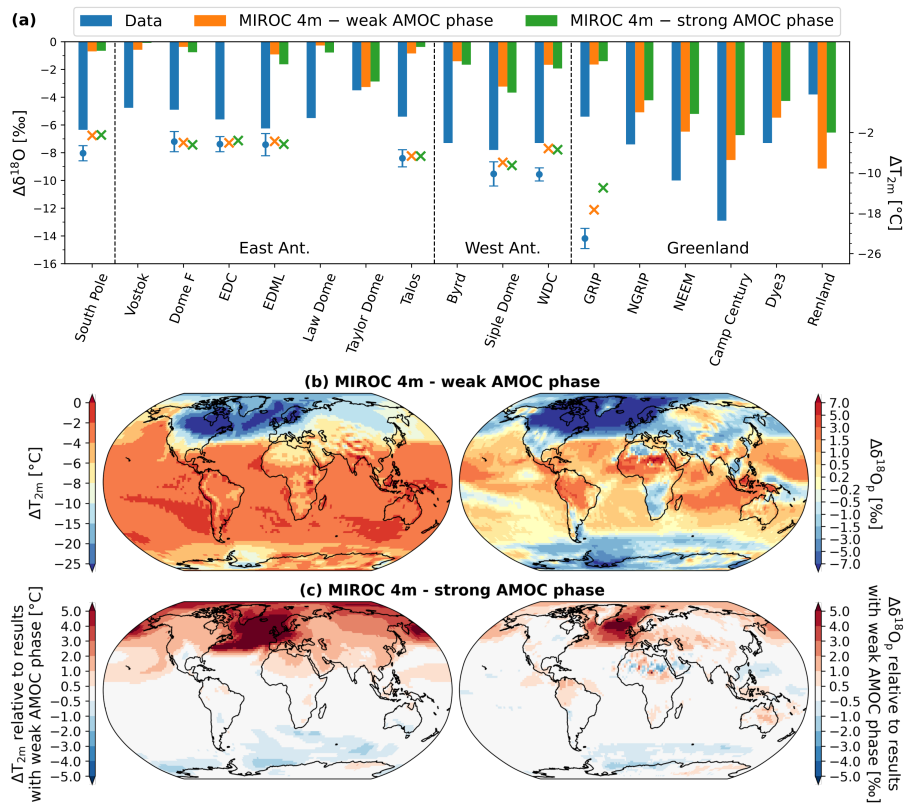
Figure 7: (a) Comparison of modeled anomalies in T_{2m} (crosses, right vertical axis) and $\delta^{18}O_{sn}$ (bars, left vertical axis) between LGM
345 and PI with temperature and δ^{18}O anomalies from polar ice cores (blue dots and bars, respectively). Modeled results are from simulations using the sea surface boundary conditions from the MIROC 4m coupled simulations: LGM_miroc4m_sst_and_sic and LGM_miroc4m_strong_AMOC_sst_and_sic in orange and green, respectively. (b) Modeled T_{2m} and $\delta^{18}O_p$ changes between LGM and PI using MIROC 4m (weak AMOC phase) sea surface boundary conditions (left and right maps, respectively). Maps in (c) show the impacts on T_{2m} and $\delta^{18}O_p$ anomalies using sea surface boundary conditions from MIROC 4m at strong LGM AMOC phase.
350 Values are expressed relative to the modeled results from (b).

4 Impacts of sea surface boundary conditions on δ^{18}O-T_{2m} temporal slope for LGM-PI climate change

We have analyzed the effects of LGM to PI changes in SST and sea ice distribution on modeled ΔT_{2m} and $\Delta\delta^{18}$O of precipitation and snow in the polar regions, as well as the impacts of the LGM AMOC strength. Next, we investigate the repercussions on modeled $\delta^{18}O_p$-T_{2m} temporal slopes and the underlying causes in terms of changes in moisture transport. In other words, are T_{2m} and δ^{18}O signals in the polar regions influenced by LGM to PI changes in SST and sea ice distribution in the same way? What are the underlying dynamics, for example, in terms of changes in concentrations and transport of water vapor? A correction for the prescribed glacial seawater change of 1 ‰ has been applied to LGM δ^{18}O values before temporal slope calculation, according to equation 1 of Stenni et al. (2010). As in Cauquoin et al. (2019b), the calculation of temporal slopes was restricted to grid cells where simulated annual mean temperatures are below +20°C for both PI and LGM. Moreover, we selected only the grid cells showing an absolute LGM-PI annual mean T_{2m} difference of at least of 0.5°C. As a comparative point, PI spatial $\delta^{18}O_p$-T_{2m} slopes of 0.72 and 0.94 ‰ °C^{-1} are modeled by ECHAM6-wiso in East and West Antarctic ice core stations, respectively (calculated by considering the 25 grid cells centered on each drill location, excluding the ocean grid points), consistent with the mean observed value of 0.8 ‰ °C^{-1} (Masson-Delmotte et al., 2008) and previous modeling studies (Schmidt et al., 2007, Werner et al., 2018, Cauquoin et al., 2019b). For Greenland ice core stations, we find a modeled spatial slope of 0.71 ‰ °C^{-1}, also in agreement with previous model results (Schmidt et al., 2007, Cauquoin et al., 2019b).

4.1 Antarctica

δ^{18}O in coastal and western low-elevated sites are derived from nearby local sources while the sources of high-elevation East Antarctic ice cores are typically further north around 40-45° S (Sodemann and Stohl, 2009). So, the values of $\delta^{18}O_p$-T_{2m} slope in Antarctica are expected to be influenced by sea surface boundary conditions in different ways depending on the ice core locations and topography.
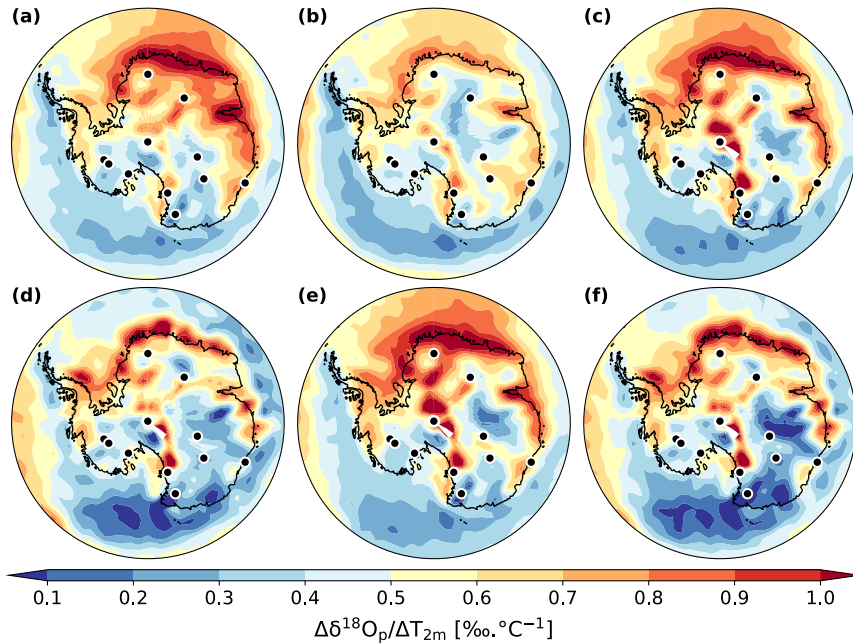
Figure 8: Spatial distribution of δ18Op-T2m temporal slope in Antarctica for LGM-PI changes according to our different ECHAM6-wiso simulations: (a) LGM_GLOMAP, (b) LGM_tierney2020, (c) LGM_miroc4m_sst_glomap_sic, (d) LGM_miroc4m_sst_and_sic, (e) LGM_miroc4m_strong_AMOC_sst_glomap_sic, and (f) LGM_miroc4m_strong_AMOC_sst_and_sic. The dots indicate the location of the ice core stations.

Greater SST cooling in the Southern Ocean influences both the LGM T_{2m} and $\delta^{18}O_p$ in the same direction (i.e., toward lower values) but with different magnitudes. Stronger cooling in the eastern part of the ocean (Tierney et al. LGM SST colder than the GLOMAP one) increases the temporal slopes at EDC and Talos Dome by 0.23 and 0.07 ‰ °C^{-1}, respectively. A higher cooling in the Atlantic sector of the Southern Ocean (GLOMAP SST in Figure 8a) makes the Antarctic temporal slope values higher between 0 and 90°E longitude compared to the other simulations. It impacts especially the Dome Fuji and EDML ice core sites, where values of temporal $\delta^{18}O_p$-T_{2m} slopes reach 0.66 and 0.69 ‰ °C^{-1}, representing an increase of at least 25% compared to simulations using SST with less cooling. This can be explained by a change in moisture transport. With a stronger SST cooling in the Southern Ocean (GLOMAP against MIROC 4m), the westerlies around Antarctica are enhanced and the atmosphere is wetter in the mid-latitudes while a drier belt appears around the continent (Figure 9b). More water vapor from the Atlantic sector at 30-40°S, where the cooling is less strong (compared to MIROC 4m SST) and the water vapor more depleted in $\delta^{18}O$ (Figure S4a) because of enhanced evaporation, is transported to eastern Antarctica. As a consequence, the larger cooling in GLOMAP Southern Ocean SST increases the temporal slope at Dome Fuji and EDML stations. A larger SST cooling near the Amundsen Sea (i.e., Tierney et al. SST compared to GLOMAP, Figure 5c) decreases the water vapor transport from this region to western Antarctica sites (Figure S7). The $\delta^{18}O$ change of the water vapor from this source area is relatively weaker (2 ‰ at maximum, right map of Figure 5c) compared to the decrease in local temperature (2 to 4 °C, left map of Figure 5c). So, less contribution from this source region to West Antarctica inland increases the temporal slopes by ~0.1 ‰ °C^{-1} at

WDC and Byrd stations (orange marker in Figure 12). At the same time, this water vapor influences the $\delta^{18}O_p$ of nearby coastal regions like the Antarctic peninsula, making decrease their temporal slopes (Figure 8b and orange marker in Figure S9).

395 LGM to PI changes in sea ice area fractions have a strong impact on the slopes in coastal regions as shown by the comparison between the plots (c)-(d) and (e)-(f) of Figure 8. Law Dome ice core is representative of this impact in coastal areas, with a slope of 0.35 and 0.64 ‰ °C^{-1} depending if a less extensive sea ice (LGM_miroc4m_sst_and_sic, Figure 8d) or a more extensive one (LGM_miroc4m_sst_glomap_sic, Figure 8c) is used, respectively. A more extensive sea ice in the Atlantic and eastern part of the Southern Ocean changes the transport of vapor only slightly (Figure 9c). On the other hand, the presence of more sea ice covered area close to the continent increases the amount of local water vapor depleted in $\delta^{18}O$ (compared to the

400 $\delta^{18}O$ of open seawater) that influences the isotopic composition of snow in coastal sites, increasing their temporal slopes. A more extensive sea ice increases the slope in a geographical band from Law Dome to Vostok and EDC stations (Figures 8c and d). This can be explained by a decrease of water vapor transport with higher $\delta^{18}O$ concentrations from the Indian Ocean and the south of Australia especially in austral winter (Figure S9). On average, the modeled temporal $\delta^{18}O_p$-T_{2m} slopes of East Antarctic ice core stations are increased by more than 25% when a more extensive sea ice is used (Figure 12, dark and light

405 purple markers against the red and grey ones, respectively). This conclusion remains the same when using the average slope across the entire East Antarctic area but with an enhanced difference because the entire coastal area is under consideration (Figure S9). No clear influence of sea ice extent on temporal slopes at West Antarctica ice core stations is found (Figure 12). On the other hand, effects in the Antarctic peninsula, Ronne Ice Shelf and on the coast of the Amundsen Sea (Figure 8), influencing the average slope values in the entire western part of the continent (Figure S9), are simulated. These are due to

410 changes in the nature of the water source nearby (i.e., open water or sea ice) depending if the sea ice used is less extensive or not.
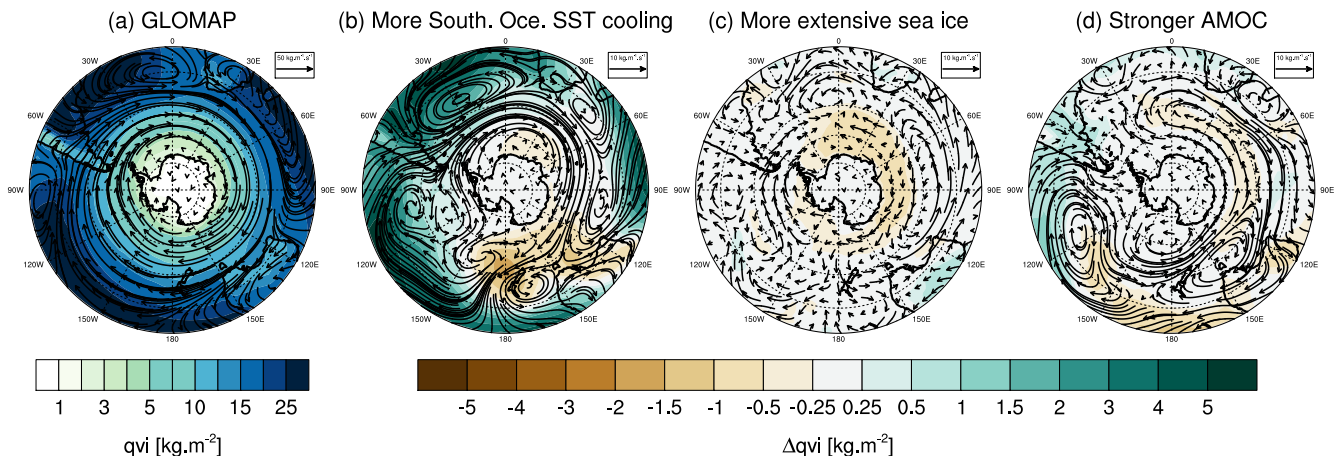
Figure 9: (a) Vertically integrated water vapor transport (arrows) and total column water vapor (qvi, colored background) in **LGM_GLOMAP** simulation over Antarctic region. Anomalies in transport and concentration of moisture are shown for **(b)** a
415 stronger SST cooling in the Southern Ocean (LGM_GLOMAP − LGM_miroc4m_sst_glomap_sic), **(c)** a more extensive sea ice (LGM_miroc4m_sst_glomap_sic − LGM_miroc4m_sst_and_sic) and **(d)** a stronger LGM AMOC (LGM_miroc4m_strong_AMOC_sst_and_sic − LGM_miroc4m_sst_and_sic).

4.2 Greenland

Using a SST field with more LGM cooling off the coast of Greenland and in the Northern North Atlantic Ocean (GLOMAP)
as forcing for ECHAM6-wiso, we model higher $\delta^{18}O_p$-T_{2m} temporal slope values at all Greenland ice core stations (Figure
10a) compared to all other simulations. The average of the temporal slope values at ice core stations is 0.50 ‰ °C^{-1} with
GLOMAP sea surface boundary forcing (blue marker in Figure 12), and less than 0.42 ‰ °C^{-1} in the other ECHAM6-wiso
simulations. This difference is enhanced by considering the entire Greenland area (blue marker in Figure S9). For Greenland,
most of the moisture comes from Northern North Atlantic Ocean at latitudes 30-40° N (Drumond et al., 2016), south of the ice
sheet (Figure 11a). A stronger SST cooling in the Arctic – North Atlantic enhances the transport of isotopically depleted water
vapor from northern USA (Figure 11b) and strengthens the water vapor transport belt around Iceland. Also, ECHAM6-wiso
simulates a slight decrease in local water vapor content in the Greenland Sea (with lower LGM $\delta^{18}O$ because the cooling is
stronger there) and its transport to the land. It increases the isotope-temperature temporal slope from the sea to inland, passing
through the eastern Greenland coast where Renland station is located (Figures 10b and 10c compared to Figure 10a).
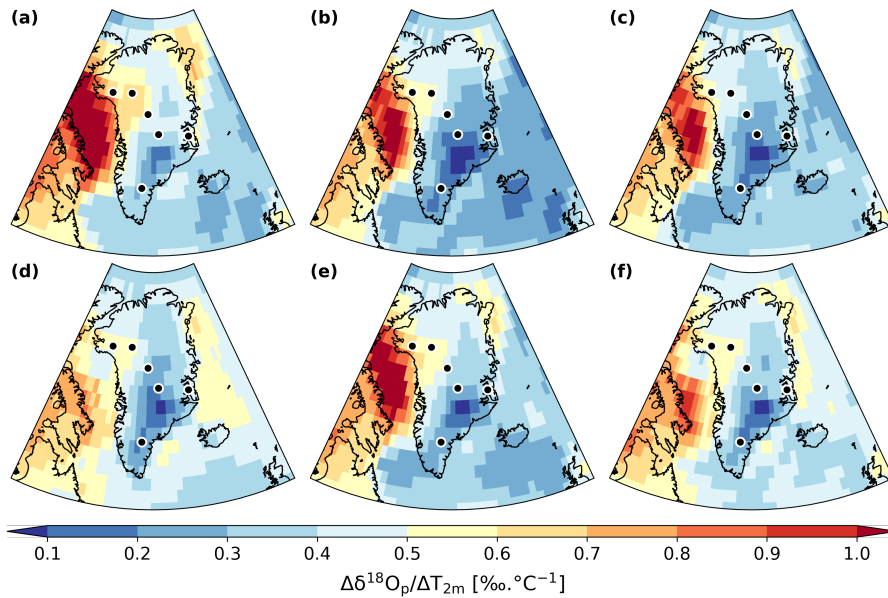
Figure 10: Same as Figure 8 but for the Greenland region.

A more extensive sea ice (i.e., MIROC 4m compared to GLOMAP) makes the Arctic Ocean area drier, especially at 50° N,
and it slightly slows down the transport of water vapor from the North Atlantic to Greenland area (Figure 11c). On the other
hand, all this area is covered by sea ice in the "more extensive sea ice" simulation (i.e., MIROC 4m sea ice). It decreases the
$\delta^{18}O$ of water vapor above this surface, increasing the isotope-temperature temporal slope on the eastern Greenland coast and
in the Greenland Sea (Figures 10d and 10f compared to Figures 10c and 10e, respectively). In the latter, a more extensive sea
ice, especially in summer, decreases the LGM $\delta^{18}O$ too, while the effect on temperature is small, again increasing the local

temporal slope. It has a slight effect on modeled temporal slopes (~0.1 ‰ °C^{-1}) over the eastern coastal regions of Greenland, including Renland station. In ECHAM6-wiso, the isotopic composition of sea ice surfaces also reflects the isotopic composition of snow deposited on this surface. Then the formation of new sea ice from PI to LGM acts as a positive feedback effect in the decrease of surrounding $\delta^{18}O_p$, leading to steeper modeled $\delta^{18}O_p$-T_{2m} temporal slopes (see Text S1 in Supplementary Material and Figure S10). Finally, ECHAM6-wiso forced with MIROC 4m sea ice, whose fractional areas are artificially lower (i.e., not 100% sea ice covered) in coastal grid cells, simulates lower $\delta^{18}O_p$-T_{2m} temporal slope values over Baffin Bay (between 0.3 and 0.9 ‰ °C^{-1}, Figures 9d and 9f) compared to when the model is forced with GLOMAP sea ice (between 0.6 and 1.25 ‰ °C^{-1}, Figures 10c and 10e). If the MIROC 4m sea ice is corrected by setting sea ice fraction as 100‰ as in GLOMAP (see Text S1 in Supplementary Material and Figure S11), we obtain temporal slope values similar to those in the simulations forced by GLOMAP sea ice (Figure S12).

A stronger AMOC increases the amount of water vapor and enhances its transport from the North Atlantic to European coastal areas because of the less extensive sea ice (Figure 11d). More water vapor with higher $\delta^{18}O$ is present southeast of Greenland because sea ice is replaced by open water. However, there is only a slight increase in the transport of this water vapor toward north in the Greenland interior (Figure 11d) while the cooling inland is largely reduced (Figure 7c). So, isotope-temperature temporal slopes are slightly increased over the interior of Greenland for stronger AMOC (dark and light purple markers in Figures 12 and S9). On the other hand, temporal slopes are decreased over the Greenland Sea (Figure 10f) because of the presence of open water instead of sea ice, enhancing the LGM $\delta^{18}O_p$ locally. Note that stronger AMOC worsens the model-data agreement for both ΔT_{2m} and $\Delta \delta^{18}O$ (Figure 7a).
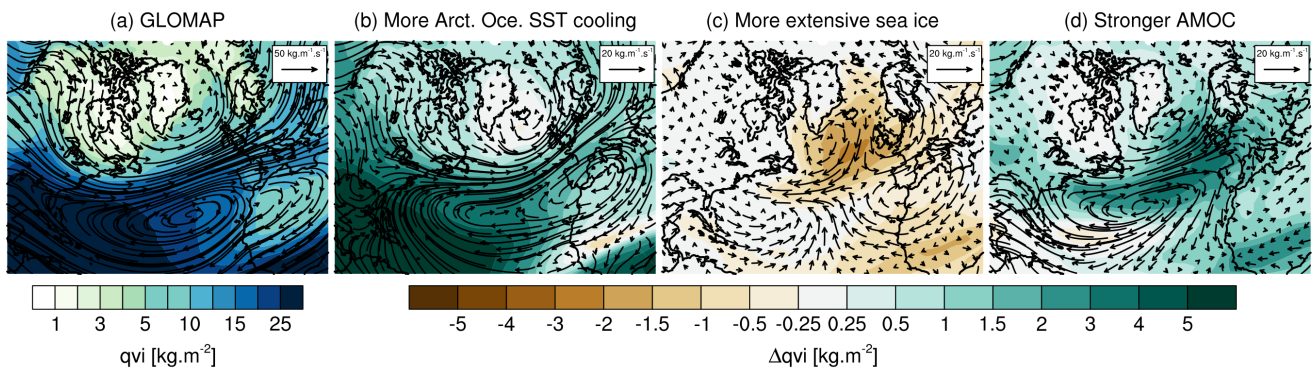
Figure 11: (a) Vertically integrated water vapor transport (arrows) and total column water vapor (qvi, colored background) in LGM_GLOMAP simulation over Arctic region. Anomalies in transport and concentration of moisture are shown for (b) a stronger SST cooling in Arctic Ocean (LGM_GLOMAP − LGM_tierney2020), (c) a more extensive sea ice (LGM_miroc4m_sst_and_sic − LGM_miroc4m_sst_glomap_sic) and (d) a stronger LGM AMOC (LGM_miroc4m_strong_AMOC_sst_and_sic − LGM_miroc4m_sst_and_sic).
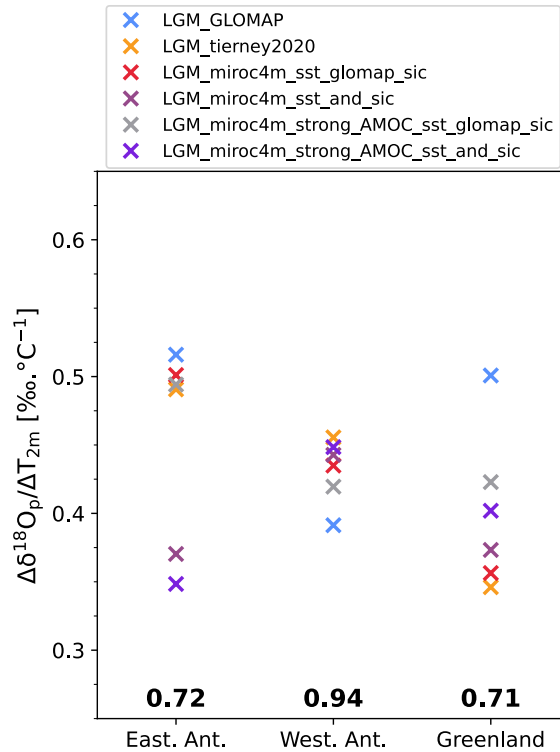
Figure 12: Average modeled values of $\delta^{18}O_p$-T_{2m} temporal slope for East Antarctic, West Antarctic and Greenland ice core stations according to our different simulations. Numbers in bold are the values of the corresponding modeled mean PI spatial slopes.

5 Conclusions and Perspectives

In this study, we elevated the importance of sea surface boundary conditions on the relationship between near-surface air temperature and $\delta^{18}O_p$ for LGM to PI climate change. Figure 13 illustrates the main findings of our study. In Antarctica, the temporal slopes in coastal area like the Antarctic peninsula, the Ronne Ice Shelf, near the Amundsen Sea and the eastern coast are influenced by sea ice extent. For example, ECHAM6-wiso simulates almost a doubling in the value of the temporal slope at Law Dome and a better isotopic model-data agreement if more extensive sea ice is used instead of the less extensive one (Figures 8c (GLOMAP sea ice) and 8d (MIROC 4m), respectively). The transport of moisture to Antarctica is generally changed only slightly changed with variations in the sea ice extent. On the other hand, the distribution of open water and sea ice covered areas around the continent mainly control the nearby $\delta^{18}O_p$ and so the isotope-temperature temporal slopes. We found that temporal slope further inland, at the EDC and Vostok sites, are influenced by changes in sea ice extent through a weakening of moisture transport from the Indian Ocean and the south of Australia when sea ice is more extensive (left map Figure 13). The values of $\delta^{18}O_p$-T_{2m} temporal slopes in inland East Antarctic ice core stations like Dome F, EDML, EDC, and Talos are mainly controlled by the change of SST in our ECHAM6-wiso simulations. Stronger cooling in the Atlantic sector of the Southern Ocean (GLOMAP) leads to steeper temporal slopes in Dome F and EDML due to enhanced water vapor

480   transport from lower latitudes. Strong cooling in the Admunsen Sea weakens the transport of relatively less depleted water vapor (compared to the large cooling) inland West Antarctica. It slightly increases the temporal slopes at the WDC and Byrd sites. At the same time, this water vapor contributes to nearby coastal region, decreasing the temporal slopes there (left map of Figure 13). These various effects on the temporal slopes can complexify the interpretation of $\delta^{18}O_p$ signals in West Antarctica, depending on the sites considered. Our modeled results demonstrate clearly that the $\delta^{18}O_p$-T_{2m} temporal slopes in

485   Greenland are influenced by the sea surface temperatures very near the coasts. The greater the LGM cooling off the coast of southeast Greenland, the larger the $\delta^{18}O_p$-T_{2m} temporal slopes (right map of Figure 13) because of an enhancement in the transport of isotopically depleted moisture from the western North Atlantic Ocean. Similarly, the presence or absence of sea ice very near the coast can impact the modeled temporal slopes in some Greenland ice core stations. It has a large influence in Baffin Bay and the Greenland Sea, too. A more or less large southern extent of the sea ice (MIROC 4m in weak AMOC phase

490   or GLOMAP, respectively) has only a slight impact on modeled temporal slope values (light purple and red markers in Figure 12, respectively). Water vapor transported to the Arctic region is more depleted when sea ice is more extensive, but less is transported to the Greenland region. The seasonal variation of the sea ice distribution, especially its retreat in summer, changes the origin type of the water source (from evaporation of open water or sublimation of snow on sea ice) and so influences the $\delta^{18}O$ of local vapor contributing to the $\delta^{18}O_p$-T_{2m} temporal slopes in the eastern part of inner Greenland (right map of Figure

495   11). Finally, a stronger LGM AMOC impacts slightly the temporal slopes modeled by ECHAM6-wiso over Greenland mainly because of the changes in the sea ice distribution. Higher temporal slopes are modeled by ECHAM6-wiso mainly because the cooling in Greenland is largely reduced while changes in $\delta^{18}O$ anomalies remain localized in the Greenland Sea. Variations in the temporal slope values are located in the Greenland Sea, where the changes in surface temperature and sea ice distribution due to the AMOC strength mainly occur. For Antarctica, only small changes in surface temperature and $\delta^{18}O$ are modeled by

500   ECHAM6-wiso because the strong phase period was selected from within the middle of the AMOC peak. The impact of the precise period chosen to represent the strong AMOC phase, for example the start or the end of the interstadial, will be investigated in more detail in a future study.
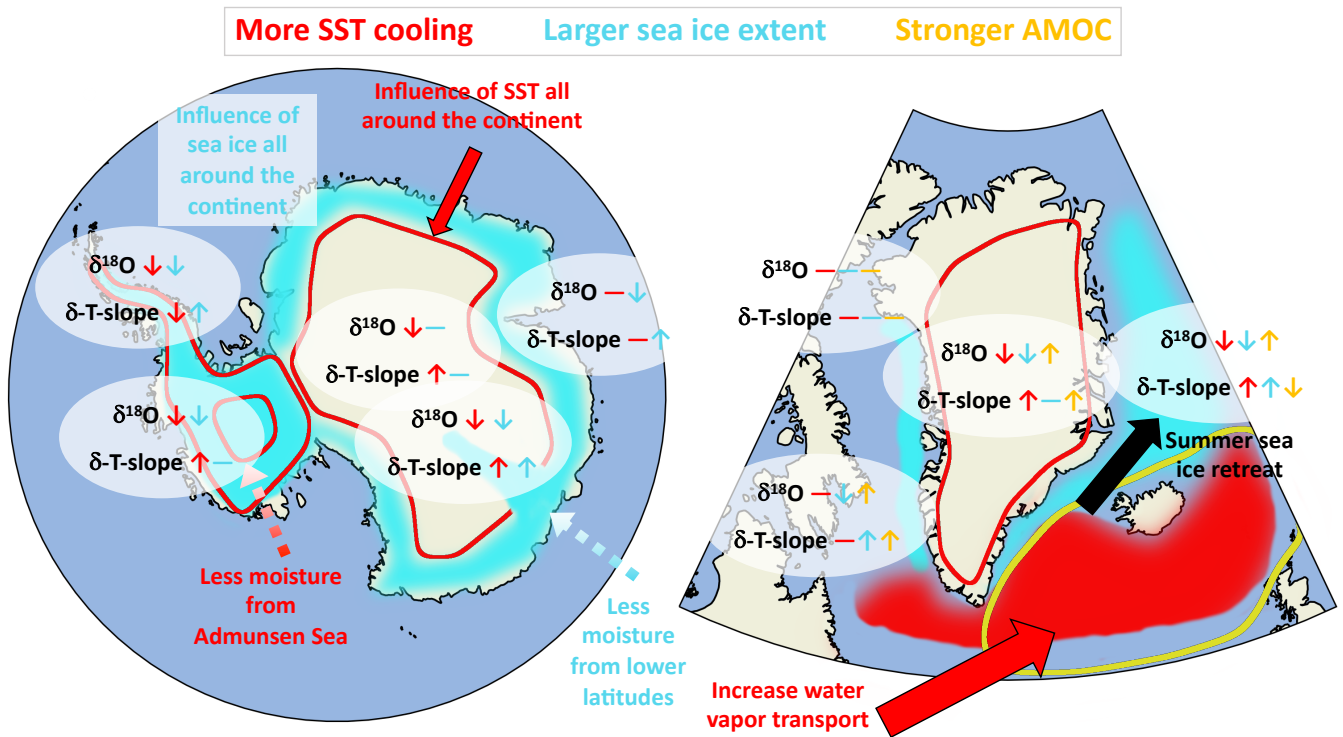
Figure 13: Summary figure illustrating the influence of higher sea surface cooling, larger sea ice extent and stronger LGM AMOC (in red, cyan and yellow, respectively) on the modeled LGM δ^{18}O and temporal δ^{18}O$_P$-T$_{2m}$ slopes in the Antarctic and Greenland regions (left and right, respectively). The up and down arrows indicate higher and lower values, respectively. The horizontal lines indicate no significant change.

In Greenland, ECHAM6-wiso simulates δ^{18}O$_P$-T$_{2m}$ temporal slopes oscillating between 0.2 and 0.7 ‰ °C^{-1} inland and at northwestern coastal sites, respectively, lower than the spatial one (0.71 ‰ °C^{-1}, Figure 12), as already reported in previous studies (Buizert et al., 2014; Cauquoin et al., 2019b; Jouzel et al., 1999; Werner et al., 2000). Our modeled temporal slope values for stations NEEM (around 0.7 ‰ °C^{-1}) and NGRIP (between 0.37 and 0.57 ‰ °C^{-1}) are in agreement with previous reconstructions (Buizert et al., 2014), too. In Antarctica, the ECHAM6-wiso modeled δ^{18}O$_P$-T$_{2m}$ temporal slopes for LGM-to-PI climate change are on average lower than the PI spatial slopes of the same model by at least 0.20 and 0.48 ‰ °C^{-1} for eastern and western ice core locations, respectively (Figure 12), regardless of the simulation being considered. By extension, we found much lower temporal slope values than the ones estimated by Buizert et al. (2021). We simulate a maximum temporal slope value of 0.9 ‰ °C^{-1} for the South Pole, while Buizert et al. (2021) found temporal slopes in Antarctic ice core stations ranging from 0.9 to 1.4 ‰ °C^{-1}, which are higher than the observed spatial δ^{18}O$_P$-T$_{2m}$ slope of 0.8 ‰ °C^{-1} (Masson-Delmotte et al., 2008). The use of the thicker PMIP3 ice sheet reconstruction compared to GLAC-1D increases the resulting modeled δ^{18}O$_P$-T$_{2m}$ temporal slopes in ECHAM6-wiso (Figure S13) with mean values for East and West Antarctic ice core stations equal to 0.68 and 0.92 ‰ °C^{-1}, respectively, by decreasing the isotopically enriched bias in the model for LGM (Figure S5). However, the temperature model-data agreement is reduced in this case. Even if ECHAM6-wiso show biases in the representation of the

isotopic content of Antarctic precipitation, we insist that the purpose of our study was to investigate the relative effects of sea surface conditions and AMOC strength on the links between $\delta^{18}O_p$ and near-surface air temperature, regardless of agreement or disagreement with other slope reconstructions.

525 In addition to orography effects, fractionation during the sublimation of surface ice is not taken into account in ECHAM6-wiso as in many isotope-enabled AGCMs. This process would lead to a further decrease in the $\delta^{18}O$ of water vapor in the polar regions, contributing to steeper modeled $\delta^{18}O_p$-T_{2m} temporal slopes in regions with low temperature. The mismatch between our model slopes and the reconstructed ones from Buizert et al. (2021) could be related to the representation of the atmospheric boundary layer and the related inversion temperature (Krinner et al., 1997; Masson-Delmotte et al., 2006; Cauquoin et al.,

530 2019a), too. Still, despite these biases that potentially affect our modeled $\delta^{18}O_p$-T_{2m} temporal slopes for LGM-to-PI climate change, our ensemble of simulations provides information on how sea surface conditions partially control the links between $\delta^{18}O_p$ and near-surface air temperature in the polar regions, through changes in the sources or transport of moisture arriving at the poles.

Because only ECHAM6-wiso is used in this study, we cannot exclude the model-dependency of our results. So, the use of

535 isotope-enabled AGCMs other than ECHAM6-wiso would be beneficial to confirm or refute our findings. A set of SST reconstructions for the LGM, based on both model results and observations, are now available. We stress the importance of providing sea ice cover reconstruction, which contributes not only to the $\delta^{18}O_p$ of coastal sites but also of some inland ice core stations, for this period too. The sea ice cover simulated by coupled GCMs for the LGM period takes various forms. An alternative reconstruction to the GLOMAP one, also based on observations, would help to better assess the impact of sea ice

540 cover on the $\delta^{18}O_p$-T_{2m} relationship for LGM to PI climate change. We also emphasize that more proxy measurements of temperature and sea ice are necessary for the Southern Ocean. Relatively large uncertainties remain in the reconstruction of the climatology in this area while the water vapor from this region contributes largely to $\delta^{18}O_p$ in Antarctica. As a first step, the focus of this study was to identify and quantify the important factors influencing the isotope-temperature relationship in the polar areas for the LGM to PI climate change. Future studies will investigate the evolution of this relationship along the

545 whole of the last deglaciation. For that, an ensemble of equilibrium isotopic simulations using the sea surface and ice sheet boundary conditions from MIROC 4m for different time periods between the LGM and PI will be performed.

Code availability. The ECHAM model code is available under a version of the MPI-M software license agreement (https://www.mpimet.mpg.de/en/science/models/license/). The code of the isotopic version ECHAM6-wiso is available upon

550 request on the AWI's GitLab repository (https://gitlab.awi.de/mwerner/mpi-esm-wiso).

Author contributions. AC designed the model experiments and performed the simulations using the MIROC 4m sea surface boundary conditions with the help of AAO, TO and WLC. AC performed the simulations using the GLOMAP or Tierney et

al. sea surface boundary conditions with the help of MW and AP. AC and all the co-authors analyzed the model outputs. AC
wrote the manuscript with contributions from all co-authors.

Competing interests. One of the co-author (André Paul) is editor in Climate of the Past.

Acknowledgements. We thank the two anonymous reviewers for their useful suggestions and comments that helped to improve substantially this article. This research was supported by JSPS KAKENHI Grant (17H06323) and by the German Federal Ministry of Education and Research (BMBF) as Research for Sustainability initiative (FONA). The ECHAM6-wiso simulations were performed at the Alfred Wegener Institute (AWI) supercomputing center. The MIROC 4m simulation used in this study was performed on the Earth Simulator 3 at Japan Agency for Marine-Earth Science and Technology (JAMSTEC).

References

Abe-Ouchi, A., Saito, F., Kawamura, K., Raymo, M. E., Okuno, J., Takahashi, K., and Blatter, H.: Insolation-driven 100,000-year glacial cycles and hysteresis of ice-sheet volume, Nature, 500, 190–193, https://doi.org/10.1038/nature12374, 2013.

Blunier, T. and Brook, E. J.: Timing of Millennial-Scale Climate Change in Antarctica and Greenland During the Last Glacial Period, Science, 291, 109–112, https://doi.org/10.1126/science.291.5501.109, 2001.

Brady, E., Stevenson, S., Bailey, D., Liu, Z., Noone, D., Nusbaumer, J., Otto-Bliesner, B. L., Tabor, C., Tomas, R., Wong, T., Zhang, J., and Zhu, J.: The Connected Isotopic Water Cycle in the Community Earth System Model Version 1, J. Adv. Model. Earth Syst., 11, 2547–2566, https://doi.org/10.1029/2019MS001663, 2019.

Briggs, R. D., Pollard, D., and Tarasov, L.: A data-constrained large ensemble analysis of Antarctic evolution since the Eemian, Quat. Sci. Rev., 103, 91–115, https://doi.org/10.1016/j.quascirev.2014.09.003, 2014.

Buizert, C., Gkinis, V., Severinghaus, J. P., He, F., Lecavalier, B. S., Kindler, P., Leuenberger, M., Carlson, A. E., Vinther, B., Masson- Delmotte, V., White, J. W. C., Liu, Z., Otto-Bliesner, B., and Brook, E. J.: Greenland temperature response to climate forcing during the last deglaciation, Science, 345, 1177–1180, https://doi.org/10.1126/science.1254961, 2014.

Buizert, C., Fudge, T. J., Roberts, W. H. G., Steig, E. J., Sherriff-Tadano, S., Ritz, C., Lefebvre, E., Edwards, J., Kawamura, K., Oyabu, I., Motoyama, H., Kahle, E. C., Jones, T. R., Abe-Ouchi, A., Obase, T., Martin, C., Corr, H., Severinghaus, J. P., Beaudette, R., Epifanio, J. A., Brook, E. J., Martin, K., Chappellaz, J., Aoki, S., Nakazawa, T., Sowers, T. A., Alley, R. B., Ahn, J., Sigl, M., Severi, M., Dunbar, N. W., Svensson, A., Fegyveresi, J. M., He, C., Liu, Z., Zhu, J., Otto-Bliesner, B. L., Lipenkov, V. Y., Kageyama, M., and Schwander, J.: Antarctic surface temperature and elevation during the Last Glacial Maximum, Science, 372, 1097–1101, https://doi.org/10.1126/science.abd2897, 2021.

585 Casado, M., Landais, A., Picard, G., Münch, T., Laepple, T., Stenni, B., Dreossi, G., Ekaykin, A., Arnaud, L., Genthon, C., Touzeau, A., Masson-Delmotte, V., and Jouzel, J.: Archival processes of the water stable isotope signal in East Antarctic ice cores, The Cryosphere, 12, 1745–1766, https://doi.org/10.5194/tc-12-1745-2018, 2018.

Cauquoin, A. and Werner, M.: High-Resolution Nudged Isotope Modeling With ECHAM6-Wiso: Impacts of Updated Model Physics and ERA5 Reanalysis Data, J. Adv. Model. Earth Syst., 13, https://doi.org/10.1029/2021MS002532, 2021.

590 Cauquoin, A., Landais, A., Raisbeck, G. M., Jouzel, J., Bazin, L., Kageyama, M., Peterschmitt, J.-Y., Werner, M., Bard, E., and ASTER Team: Comparing past accumulation rate reconstructions in East Antarctic ice cores using [10]Be, water isotopes and CMIP5-PMIP3 models, Clim. Past, 11, 355–367, https://doi.org/10.5194/cp-11-355-2015, 2015.

Cauquoin, A., Risi, C., and Vignon, É.: Importance of the advection scheme for the simulation of water isotopes over Antarctica by atmospheric general circulation models: A case study for present-day and Last Glacial Maximum with LMDZ-iso, 595 Earth and Planet. Sci. Lett., 524, 115 731, https://doi.org/10.1016/j.epsl.2019.115731, 2019a.

Cauquoin, A., Werner, M., and Lohmann, G.: Water isotopes – climate relationships for the mid-Holocene and preindustrial period simulated with an isotope-enabled version of MPI-ESM, Clim. Past, 15, 1913–1937, https://doi.org/10.5194/cp-15-1913-2019, 2019b.

Comas-Bru, L., Rehfeld, K., Roesch, C., Amirnezhad-Mozhdehi, S., Harrison, S. P., Atsawawaranunt, K., Ahmad, S. M., 600 Brahim, Y. A., Baker, A., Bosomworth, M., Breitenbach, S. F. M., Burstyn, Y., Columbu, A., Deininger, M., Demény, A., Dixon, B., Fohlmeister, J., Hatvani, I. G., Hu, J., Kaushal, N., Kern, Z., Labuhn, I., Lechleitner, F. A., Lorrey, A., Martrat, B., Novello, V. F., Oster, J., Pérez-Mejías, C., Scholz, D., Scroxton, N., Sinha, N., Ward, B. M., Warken, S., and Zhang, H.: SISALv2: a comprehensive speleothem isotope database with multiple age–depth models, Earth Syst. Sci. Data, 12, 2579–2606, https://doi.org/10.5194/essd-12-2579-2020, 2020.

605 Craig, H.: Isotopic Variations in Meteoric Waters, Science, 133, 1702–1703, https://doi.org/10.1126/science.133.3465.1702, 1961.

Craig, H. and Gordon, L. I.: Deuterium and oxygen 18 variation in the ocean and marine atmosphere, in: Stable Isotopes in Oceanographic Studies and Paleotemperatures, edited by Tongiogi, E., pp. 9–130, Consiglio nazionale delle richerche, Laboratorio de geologia nucleare, Spoleto, Italy, 1965.

610 Dahl-Jensen, D., Mosegaard, K., Gundestrup, N., Clow, G. D., Johnsen, S. J., Hansen, A. W., and Balling, N.: Past Temperatures Directly from the Greenland Ice Sheet, Science, 282, 268–271, https://doi.org/10.1126/science.282.5387.268, 1998.

Dansgaard, W.: Stable isotopes in precipitation, Tellus, 16, 436–468, https://doi.org/10.3402/tellusa.v16i4.8993, 1964.

Drumond, A., Taboada, E., Nieto, R., Gimeno, L., Vicente-Serrano, S. M., and López-Moreno, J. I.: A Lagrangian analysis of 615 the present-day sources of moisture for major ice-core sites, Earth Syst. Dynam., 7, 549–558, https://doi.org/10.5194/esd-7-549-2016, 2016.

Eyring, V., Bony, S., Meehl, G. A., Senior, C. A., Stevens, B., Stouffer, R. J., and Taylor, K. E.: Overview of the Coupled Model Intercom- parison Project Phase 6 (CMIP6) experimental design and organization, Geosci. Model Dev., 9, 1937–1958, https://doi.org/10.5194/gmd-9-1937-2016, 2016.

620 Giorgetta, M. A., Jungclaus, J., Reick, C. H., Legutke, S., Bader, J., Böttinger, M., Brovkin, V., Crueger, T., Esch, M., Fieg, K., Glushak, K., Gayler, V., Haak, H., Hollweg, H.-D., Ilyina, T., Kinne, S., Kornblueh, L., Matei, D., Mauritsen, T., Mikolajewicz, U., Mueller, W., Notz, D., Pithan, F., Raddatz, T., Rast, S., Redler, R., Roeckner, E., Schmidt, H., Schnur, R., Segschneider, J., Six, K. D., Stockhause, M., Timmreck, C., Wegner, J., Widmann, H., Wieners, K.-H., Claussen, M., Marotzke, J., and Stevens, B.: Climate and carbon cycle changes from 1850 to 2100 in MPI-ESM
625 simulations for the Coupled Model Intercomparison Project phase 5, J. Adv. Model. Earth Syst., 5, 572–597, https://doi.org/10.1002/jame.20038, 2013.

Guillevic, M., Bazin, L., Landais, A., Kindler, P., Orsi, A., Masson-Delmotte, V., Blunier, T., Buchardt, S. L., Capron, E., Leuenberger, M., Martinerie, P., Prié, F., and Vinther, B. M.: Spatial gradients of temperature, accumulation and δ18O-ice in Greenland over a series of Dansgaard–Oeschger events, Clim. Past, 9, 1029–1051, https://doi.org/10.5194/cp-9-
630 1029-2013, 2013.

Jouzel, J.: Calibrating the Isotopic Paleothermometer, Science, 286, 910–911, https://doi.org/10.1126/science.286.5441.910, 1999.

Jouzel, J.: A brief history of ice core science over the last 50 yr, Clim. Past, 9, 2525–2547, https://doi.org/10.5194/cp-9-2525-2013, 2013.

635 Jouzel, J., Masson-Delmotte, V., Cattani, O., Dreyfus, G., Falourd, S., Hoffmann, G., Minster, B., Nouet, J., Barnola, J.-M., Blunier, T., Chappellaz, J., Fischer, H., Gallet, J. C., Johnsen, S., Leuenberger, M., Loulergue, L., Luethi, D., Oerter, H., Parrenin, F., Raisbeck, G., Raynaud, D., Schilt, A., Schwander, J., Delmo, E., Souchez, R., Spahni, R., Stauffer, B., Steffensen, J. P., Stenni, B., Stocker, T. F., Tison, J. L., Werner, M., and Wolff, E.: Orbital and Millennial Antarctic Climate Variability over the Past 800,000 Years, Science, 317, 793–796, https://doi.org/10.1126/science.1141038,
640 2007.

Kageyama, M., Braconnot, P., Harrison, S. P., Haywood, A. M., Jungclaus, J. H., Otto-Bliesner, B. L., Peterschmitt, J.-Y., Abe-Ouchi, A., Albani, S., Bartlein, P. J., Brierley, C., Crucifix, M., Dolan, A., Fernandez-Donado, L., Fischer, H., Hopcroft, P. O., Ivanovic, R. F., Lambert, F., Lunt, D. J., Mahowald, N. M., Peltier, W. R., Phipps, S. J., Roche, D. M., Schmidt, G. A., Tarasov, L., Valdes, P. J., Zhang, Q., and Zhou, T.: The PMIP4 contribution to CMIP6 – Part 1:
645 Overview and over-arching analysis plan, Geosci. Model Dev., 11, 1033–1057, https://doi.org/10.5194/gmd-11-1033-2018, 2018.

Kageyama, M., Harrison, S. P., Kapsch, M.-L., Lofverstrom, M., Lora, J. M., Mikolajewicz, U., Sherriff-Tadano, S., Vadsaria, T., Abe-Ouchi, A., Bouttes, N., Chandan, D., Gregoire, L. J., Ivanovic, R. F., Izumi, K., LeGrande, A. N., Lhardy, F., Lohmann, G., Morozova, P. A., Ohgaito, R., Paul, A., Peltier, W. R., Poulsen, C. J., Quiquet, A., Roche, D. M., Shi,
650 X., Tierney, J. E., Valdes, P. J., Volodin, E., and Zhu, J.: The PMIP4 Last Glacial Maximum experiments: preliminary

results and comparison with the PMIP3 simulations, Clim. Past, 17, 1065–1089, https://doi.org/10.5194/cp-17-1065-2021, 2021.

Kawamura, K., Parrenin, F., Lisiecki, L., Uemura, R., Vimeux, F., Severinghaus, J. P., Hutterli, M. A., Nakazawa, T., Aoki, S., Jouzel, J., Raymo, M. E., Matsumoto, K., Nakata, H., Motoyama, H., Fujita, S., Goto-Azuma, K., Fujii, Y., and Watanabe, O.: Northern Hemisphere forcing of climatic cycles in Antarctica over the past 360,000 years, Nature, 448, 912–916, https://doi.org/10.1038/nature06015, 2007.

Krinner, G., Genthon, C., Li, Z.-X., and Le Van, P.: Studies of the Antarctic climate with a stretched-grid general circulation model, J. Geophys. Res. Atmos., 102, 13 731–13 745, https://doi.org/10.1029/96JD03356, 1997.

Landais, A., Masson-Delmotte, V., Stenni, B., Selmo, E., Roche, D. M., Jouzel, J., Lambert, F., Guillevic, M., Bazin, L., Arzel, O., Vinther, B., Gkinis, V., and Popp, T.: A review of the bipolar see-saw from synchronized and high resolution ice core water stable isotope records from Greenland and East Antarctica, Quat. Sci. Rev., 114, 18–32, https://doi.org/10.1016/j.quascirev.2015.01.031, 2015.

Lee, J.-E., Fung, I., DePaolo, D. J., and Otto-Bliesner, B.: Water isotopes during the Last Glacial Maximum: New general circulation model calculations, J. Geophys. Res., 113, D19 109, https://doi.org/10.1029/2008JD009859, 2008.

LeGrande, A. N. and Schmidt, G. A.: Global gridded data set of the oxygen isotopic composition in seawater, Geophys. Res. Lett., 33, https://doi.org/10.1029/2006gl026011, 2006.

Masson-Delmotte, V., Kageyama, M., Braconnot, P., Charbit, S., Krinner, G., Ritz, C., Guilyardi, E., Jouzel, J., Abe-Ouchi, A., Crucifix, M., Gladstone, R. M., Hewitt, C. D., Kitoh, A., LeGrande, A. N., Marti, O., Merkel, U., Motoi, T., Ohgaito, R., Otto-Bliesner, B., Peltier, W. R., Ross, I., Valdes, P. J., Vettoretti, G., Weber, S. L., Wolk, F., and Yu, Y.: Past and future polar amplification of climate change: climate model intercomparisons and ice-core constraints, Clim. Dynam., 26, 513–529, https://doi.org/10.1007/s00382-005-0081-9, 2006.

Masson-Delmotte, V., Hou, S., Ekaykin, A., Jouzel, J., Aristarain, A., Bernardo, R. T., Bromwhich, D., Cattani, O., Delmotte, M., Falourd, S., Frezzotti, M., Gallée, H., Genoni, L., Isaksson, E., Landais, A., Helsen, M., Hoffmann, G., Lopez, J., Morgan, V., Motoyama, H., Noone, D., Oerter, H., Petit, J. R., Royer, A., Uemura, R., Schmidt, G. A., Schlosser, E., Simões, J. C., Steig, E., Stenni, B., Stievenard, M., van den Broeke, M., van de Wal, R., van de Berg, W.-J., Vimeux, F., and White, J. W. C.: A review of Antarctic surface snow isotopic composition: observations, atmospheric circulation and isotopic modelling, J. Climate, 21, 3359–3387, https://doi.org/10.1175/2007JCLI2139.1, 2008.

Mauritsen, T., Bader, J., Becker, T., Behrens, J., Bittner, M., Brokopf, R., Brovkin, V., Claussen, M., Crueger, T., Esch, M., Fast, I., Fiedler, S., Fläschner, D., Gayler, V., Giorgetta, M., Goll, D. S., Haak, H., Hagemann, S., Hedemann, C., Hohenegger, C., Ilyina, T., Jahns, T., la Cuesta, D. J.-d., Jungclaus, J., Kleinen, T., Kloster, S., Kracher, D., Kinne, S., Kleberg, D., Lasslop, G., Kornblueh, L., Marotzke, J., Matei, D., Meraner, K., Mikolajewicz, U., Modali, K., Möbis, B., Müller, W. A., Nabel, J. E. M. S., Nam, C. C. W., Notz, D., Nyawira, S.-S., Paulsen, H., Peters, K., Pincus, R., Pohlmann, H., Pongratz, J., Popp, M., Raddatz, T. J., Rast, S., Redler, R., Reick, C. H., Rohrschneider, T., Schemann, V., Schmidt, H., Schnur, R., Schulzweida, U., Six, K. D., Stein, L., Stemmler, I., Stevens, B., Storch, J.-S., Tian, F.,

685   Voigt, A., Vrese, P., Wieners, K.-H., Wilkenskjeld, S., Winkler, A., and Roeckner, E.: Developments in the MPI- M Earth System Model version 1.2 (MPI-ESM1.2) and Its Response to Increasing CO_2, J. Adv. Model. Earth Syst., 11, 998–1038, https://doi.org/10.1029/2018ms001400, 2019.

NEEM Community Members: Eemian interglacial reconstructed from a Greenland folded ice core, Nature, 493, 489–494, https://doi.org/10.1038/nature11789, 2013.

690   Noone, D. and Simmonds, I.: Sea ice control of water isotope transport to Antarctica and implications for ice core interpretation, J. Geophys. Res. Atmos, 109, D07 105, https://doi.org/10.1029/2003jd004228, 2004.

North Greenland Ice Core Project members: High-resolution record of Northern Hemisphere climate extending into the last interglacial period, Nature, 431, 147–151, https://doi.org/10.1038/nature02805, 2004.

Obase, T. and Abe-Ouchi, A.: Abrupt Bølling-Allerød Warming Simulated under Gradual Forcing of the Last Deglaciation,
695   Geophys. Res. Lett., 46, 11 397–11 405, https://doi.org/10.1029/2019GL084675, 2019.

Paul, A., Mulitza, S., Stein, R., and Werner, M.: A global climatology of the ocean surface during the Last Glacial Maximum mapped on a regular grid (GLOMAP), Clim. Past, 17, 805–824, https://doi.org/10.5194/cp-17-805-2021, 2021.

Schmidt, G. A., LeGrande, A. N., and Hoffmann, G.: Water isotope expressions of intrinsic and forced variability in a coupled ocean- atmosphere model, J. Geophys. Res., 112, D10103, https://doi.org/10.1029/2006JD007781, 2007.

700   Schüpbach, S., Fischer, H., Bigler, M., Erhardt, T., Gfeller, G., Leuenberger, D., Mini, O., Mulvaney, R., Abram, N. J., Fleet, L., Frey, M. M., Thomas, E., Svensson, A., Dahl-Jensen, D., Kettner, E., Kjaer, H., Seierstad, I., Steffensen, J. P., Rasmussen, S. O., Vallelonga, P., Winstrup, M., Wegner, A., Twarloh, B., Wolff, K., Schmidt, K., Goto-Azuma, K., Kuramoto, T., Hirabayashi, M., Uetake, J., Zheng, J., Bourgeois, J., Fisher, D., Zhiheng, D., Xiao, C., Legrand, M., Spolaor, A., Gabrieli, J., Barbante, C., Kang, J.-H., Hur, S. D., Hong, S. B., Hwang, H. J., Hong, S., Hansson, M.,
705   Iizuka, Y., Oyabu, I., Muscheler, R., Adolphi, F., Maselli, O., McConnell, J., and Wolff, E. W.: Greenland records of aerosol source and atmospheric lifetime changes from the Eemian to the Holocene, Nat. Commun., 9, 1476, https://doi.org/10.1038/s41467-018-03924-3, 2018.

Sime, L. C., Wolff, E. W., Oliver, K. I. C., and Tindall, J. C.: Evidence for warmer interglacials in East Antarctic ice cores, Nature, 462, 342–345, https://doi.org/10.1038/nature08564, 2009.

710   Sodemann, H., and Stohl, A.: Asymmetries in the moisture origin of Antarctic precipitation. Geophys. Res. Lett., 36(22), L22803, https://doi.org/10.1029/2009GL040242, 2009.

Steig, E. J., Morse, D. L., Waddington, E. D., Stuiver, M., Grootes, P. M., Mayewski, P. A., Twickler, M. S., and Whitlow, S. I.: Wisconsinan and Holocene climate history from an ice core at Taylor Dome, western Ross embayment, Antarctica, Geografiska Annaler, 82A, 213–235, https://doi.org/10.1111/j.0435-3676.2000.00122.x, 2000.

715   Steig, E. J., Jones, T. R., Schauer, A. J., Kahle, E. C., Morris, V. A., Vaughn, B. H., Davidge, L., and White, J. W. C.: Continuous-Flow Analysis of $\delta^{17}O$, $\delta^{18}O$, and δD of H_2O on an Ice Core from the South Pole, Front. Earth Sci., 9, https://doi.org/10.3389/feart.2021.640292, 2021.

Stenni, B., Masson-Delmotte, V., Selmo, E., Oerter, H., Meyer, H., Röthlisberger, R., Jouzel, J., Cattani, O., Falourd, S., Fischer, H., Hoff- mann, G., Iacumin, P., Johnsen, S. J., Minster, B., and Udisti, R.: The deuterium excess records of EPICA Dome C and Dronning Maud Land ice cores (East Antarctica), Quat. Sci. Rev., 29, 146–159, https://doi.org/10.1016/j.quascirev.2009.10.009, 2010.

Stenni, B., Buiron, D., Frezzotti, M., Albani, S., Barbante, C., Bard, E., Barnola, J. M., Baroni, M., Baumgartner, M., Bonazza, M., Capron, E., Castellano, E., Chappellaz, J., Delmonte, B., Falourd, S., Genoni, L., Iacumin, P., Jouzel, J., Kipfstuhl, S., Landais, A., Lemieux- Dudon, B., Maggi, V., Masson-Delmotte, V., Mazzola, C., Minster, B., Montagnat, M., Mulvaney, R., Narcisi, B., Oerter, H., Parrenin, F., Petit, J. R., Ritz, C., Scarchilli, C., Schilt, A., Schüpbach, S., Schwander, J., Selmo, E., Severi, M., Stocker, T. F., and Udisti, R.: Expression of the bipolar see-saw in Antarctic climate records during the last deglaciation, Nat. Geosci., 4, 46–49, https://doi.org/10.1038/ngeo1026, 2011.

Stevens, B., Giorgetta, M., Esch, M., Mauritsen, T., Crueger, T., Rast, S., Salzmann, M., Schmidt, H., Bader, J., Block, K., Brokopf, R., Fast, I., Kinne, S., Kornblueh, L., Lohmann, U., Pincus, R., Reichler, T., and Roeckner, E.: Atmospheric component of the MPI-M Earth System Model: ECHAM6, J. Adv. Model. Earth Syst., 5, 146–172, https://doi.org/10.1002/jame.20015, 2013.

Tarasov, L. and Peltier, W. R.: Greenland glacial history and local geodynamic consequences, Geophysical Journal International, 150, 198– 229, https://doi.org/10.1046/j.1365-246X.2002.01702.x, 2002.

Tarasov, L., Dyke, A. S., Neal, R. M., and Peltier, W. R.: A data-calibrated distribution of deglacial chronologies for the North American ice complex from glaciological modeling, Earth and Planet. Sci. Lett., 315-316, 30–40, https://doi.org/10.1016/j.epsl.2011.09.010, 2012.

Tarasov, L., Hughes, A., Gyllencreutz, R., Lohne, O. S., Mangerud, J., and Svendsen, J.-I.: The global GLAC-1c deglaciation chronology, melwater pulse 1-a, and a question of missing ice, in: IGS Symposium on Contribution of Glaciers and Ice Sheets to Sea-Level Change, 2014.

Tierney, J. E., Zhu, J., King, J., Malevich, S. B., Hakim, G. J., and Poulsen, C. J.: Glacial cooling and climate sensitivity revisited, Nature, 584, 569–573, https://doi.org/10.1038/s41586-020-2617-x, 2020.

Vinther, B. M., Andersen, K. K., Jones, P. D., Briffa, K. R., and Cappelen, J.: Extending Greenland temperature records into the late eighteenth century, J. Geophys. Res., 111, D11 105, https://doi.org/10.1029/2005jd006810, 2006.

Vinther, B. M., Buchardt, S. L., Clausen, H. B., Dahl-Jensen, D., Johnsen, S. J., Fisher, D. A., Koerner, R. M., Raynaud, D., Lipenkov, V., Andersen, K. K., Blunier, T., Rasmussen, S. O., Steffensen, J. P., and Svensson, A. M.: Holocene thinning of the Greenland ice sheet, Nature, 461, 385–388, https://doi.org/10.1038/nature08355, 2009.

WAIS Divide Project Members: Onset of deglacial warming in West Antarctica driven by local orbital forcing, Nature, 500, 440–444, https://doi.org/10.1038/nature12376, 2013.

Werner, M., Mikolajewicz, U., Heimann, M., and Hoffmann, G.: Borehole versus isotope temperatures on Greenland: Seasonality does matter, Geophys. Res. Lett., 27, 723–726, https://doi.org/10.1029/1999gl006075, 2000.

Werner, M., Jouzel, J., Masson-Delmotte, V., and Lohmann, G.: Reconciling glacial Antarctic water stable isotopes with ice sheet topography and the isotopic paleothermometer, Nat. Commun., 9, https://doi.org/10.1038/s41467-018-05430-y, 2018.